2025-05

Stapp Car Crash Journal, Vol. 69, pp. 114-161
© 2025 The Stapp Association

Assessment of the skull fracture prediction capability of finite element head models

Clément Pozzi, Marc Gardegaront, Lucille Allegre, Philippe Beillas
Univ Lyon, Univ Lyon 1, Univ Eiffel, LBMC UMR_T9406, 69622 Lyon, France

ABSTRACT – The development of drones has raised questions about their safety in case of high-speed impacts with the head. This has been recently studied with dummies, postmortem human surrogates and numerical models but questions are still open regarding the transfer of skull fracture tolerance and procedures from road safety to drone impacts.
This study aimed to assess the performance of an existing head FE model (GHBMC M50-O v6.0) in terms of response and fracture prediction using a wide range of impact conditions from the literature (low and high-speed, rigid and deformable impactors, drones). The fracture prediction capability was assessed using 156 load cases, including 18 high speed tests and 19 tests for which subject specific models were built.
The GHBMC model was found to overpredict peak forces, especially for rigid impactors and fracture cases. However, the model captured the head accelerations tendencies for drone impacts. The formulation of bone elements, the failure representation and the scalp material properties were found of interest for future investigation. The model still predicted a sizable proportion of skull fractures. With failure enabled, it reached a sensitivity of 86.6% and a specificity of 82.0% (n=156). With failure disabled, risk curves with a rating of good according to ISO/TS 18506:2014 were developed using the second principal strain in the outer table cortical solid elements.

KEYWORDS – skull fracture, finite element model, validation, risk curve, drone, high speed, subject specific models

INTRODUCTION

Injuries in drone incidents

The number of professional and personal Unmanned Aircraft Systems (UAS), or drones is increasing with time and the drone marketplace still shows an important growth potential (SESAR Joint Undertaking., 2017). Although the risk on the ground may be small as only one case of comminuted depressed vertex skull fracture following a leisure drone impact was reported in the literature (Chung et al., 2017; Khan & Brown, 2021), the prevention of skull fractures is considered in new regulations for drones potentially flying over humans. In the Unites States, a new regulation permits drones exceeding 250 grams to fly over people only if they do not subject people to a higher injury risk than a 15 J impact from a rigid object (Federal Aviation Administration, FAA, 2020). In Europe, the regulation EU 2019/947 distinguishes drone classes depending on their interaction with the head (among other criteria) and mentions that the drones of class C1 should ensure that "in the event of an impact at terminal velocity with a human head, the energy transmitted to the human head is less than 80 J" (European Union Aviation Safety Agency, EASA, 2019). However, besides questions about the scientific bases of these regulations, it is unclear how these criteria could be assessed in practice for a drone. There would be a need of procedure, surrogate, and method to assess the risk (low risks, risk equivalence for the FAA, etc.).

Drone impact speeds can be much higher (e.g. over 20 m/s) than the ones targeted by road safety regulations for which human surrogates and injury criteria were developed. Furthermore, drones have specific masses, stiffness and energy absorption characteristics which may affect the loading mechanisms and the injury outcome (e.g. Li-On battery). Most head injury

Address correspondence to: Clément Pozzi and Philippe Beillas, Univ Eiffel, LBMC, 25 av F. Mitterrand, 69675 Bron Cédex, France. Electronic mail: philippe.beillas@univ-eiffel.fr

research focuses on blunt impacts, but drones may include sharp or rigid structures that increase the risk of local fractures.

Drone impacts have been the focus of several recent biomechanical studies. Actual drones were tested against dummy heads (Arterburn et al., 2019) and PMHS (Stark et al., 2019) as part of the ASSURE program coordinated by the Federal Aviation Administration (FAA). In France, dummy tests with actuals drones were also performed up to 16 m/s (Berthe et al., 2019) as part of the Ground Impact Study (GIS) projects funded by the French Directorate General for Civil Aviation (DGAC). In worst cases, dummies Head Injury Criterion (HIC) values were higher than the lowest fracture points used in Prasad and Mertz (1985) for the establishment of the current HIC risk curves (e.g. up to 490 in GIS at 16 m/s), up to 1064 in ASSURE at 21.9 m/s). On PMHS, only one fracture was observed after repeated testing on the same PMHS. PMHS HIC values were high compared to dummy readings (e.g. 4491 without skull fracture). This could be attributed to skull deformability and vibrations for a very short impact duration. Raymond et al. (2009) who conducted high speed tests with a low mass rigid impactor indicated that based on previous studies, the short impact time could excite deformation modes affecting local accelerations (acceleration amplification, e.g. Hodgson & Thomas, 1969). The high-speed drone impacts fall within that range of duration.

Human numerical models have also been used to study the drone impacts. Multibody full body models have been used to systematically explore effects of drone mass, velocity, impact direction and structural compliance using drone airbags. However, these studies used only injury criteria for head and neck which need validation for drone impact (Rattanagraikanakorn et al., 2019, 2020a, 2020b, 2022). As they represent more closely the human anatomy than dummies and rigid body models, human body models based on the finite element methods (HBM) initially developed for road safety could be more resilient to differences of impact conditions and could better describe the loading mechanisms including for short durations. In the absence of sufficient data specific to drones to develop risk curves from scratch, HBM may be helpful to compare the tendencies in terms of responses and risk between impact conditions (e.g. low or high speed, deformable or rigid impactor). This could give an indication about the need to adjust (or not) risk assessment methods that can be developed using the large amount of data available for road safety conditions. The HBM could also be a useful surrogate to compare the risks resulting from a drone impact to the one resulting from a 15 J impact with a rigid object as defined in the FAA regulation. This would however require to predict a probability of injury based on a simulation (probabilistic criterion). Within ASSURE, the Thums (Total Human Model for Safety, Toyota Motor Company) and GHBMC (from the Global Human Body Model Consortium) head models were used to reproduce some of the impacts from Stark et al. (2019) (Arterburn et al., 2019). Weng et al. (2021) used the Thums to simulate 17 PMHS drone impacts from Stark et al. (2019) and concluded that the model was sensitive to the impact conditions in a similar manner as the PMHS. Using the GHBMC, Pozzi et al. (2022) studied skull fractures (represented by bone element elimination) when subjected to impacts with rigid or deformable impactors. They observed (1) increased fractures at high velocities for a given energy and impactor deformability and (2) a limited performance of the model HIC to separate fracture and non-fracture cases. While the sensitivity of these two HBM to conditions relevant for drone impact conditions was therefore demonstrated, there is to our knowledge no study (1) comparing their responses in conditions relevant for drones to the diversity of conditions for which data are available in the broad head impact literature and (2) providing a probabilistic assessment of the risk of skull fracture. For example, the GHBMC validation reported in Mao et al. (2013) and Lyu et al. (2022) was limited velocities below 8 m/s, and the skull fracture assessment (based on element elimination) only included rigid impactors and fracture cases from three studies. It did not include the drone results from Stark, nor the high speeds tests from Raymond et al. (at speeds similar to drones), nor impacts at low speed with deformable impactors. The objectives of this study are therefore to assess the performance of an existing head FE model (the GHBMC v6.0 already used in Pozzi et al., 2022) across a broad range of conditions in terms of (1) response/biofidelity and (2) injury prediction capability using (a) the existing element elimination approach and (b) a new probabilistic assessment of the risk of skull fracture. Conditions will include low and high velocity conditions, impacts against rigid and deformable objects including simplified drone models.

METHODS

Reference experimental studies and impact conditions

Reference data from past studies were gathered to build the database of cases to be simulated. There are numerous studies in which the head is loaded, and the presence or absence of fracture reported. The list of studies selected is therefore by no means exhaustive

but aims to cover a variety of conditions in terms of velocities, impactor stiffness, directions, and, if possible, include both injurious and non-injurious tests within the same study.

First, the conditions against which the model was validated were selected based on Mao et al., 2013 and Lyu et al., 2022. These include frontal (Allsop et al., 1988; Yoganandan et al., 1995, Hodgson et al. 1970), parietal (Allsop et al., 1991) and temporal (Allsop et al., 1991) impacts. All used rigid impactors and velocities below 8 m/s. This condition was extended by adding results from Hodgson & Thomas (1971) and Hodgson (1973). The woodblock tests (6 to 12 m/s) from Stark et al., (2019) were also added. Then, the velocity range with a rigid impactor was expanded using tests from Raymond et al., 2009) with a low mass impactor (0.103 kg) at velocities between 16.3 and 35.2 m/s.

For deformable impactors, high speed tests (over 17 m/s) from Stark et al. (2019) with two actual drones were selected (DJI Mavic Pro and Phantom 3). Adding padded tests from the literature requires modelling the padding. Two padding materials that could still be tested were selected for now: (1) Expanded Polystyrene (EPS) of known densities as they are still available on the market (2) Ensolite, which has been used in numerous studies and is still used in dummies. Tests using these materials from Got et al. (1978), Alem et al. (1984), Nusholtz et al. (1984) and McIntosh et al. (1993) were selected.

Not all tests from all studies were used for all analyses. Multiple selection criteria were applied:

- When tests were repeated on the same PMHS and same location, only the most severe non-injurious test was used for the injury analysis. Injurious results were only used if they were the first test. If the first test is injurious, then the result is used as an injury point (right censored, as the time of failure is unknown) because all damage leading to failure can be attributed to this test. For non-injurious tests, even if microdamage accumulates, it is still below the failure limit. Hence the most severe non injurious test can be used as a no injury point (left censored).
    - This applied to Hodgson et al. (1970, 1971, 1973) drop tests at 5 inches height increment and the Nusholtz et al. (1984) tests. Injurious tests from Hodgson's studies were used for force comparisons as the force was not available from previous tests.
    - This applied to the drone test from Stark et al. (2019) in which a fracture was reported: it was not considered injurious as other tests were performed in the same location before (three tests on the right side of the head, then one test in the same impact location as the injurious one).
    - This did not apply to the two tests performed on each PMHS by Raymond et al. (2009) as the tests were on opposite sides of the head and the impactor was small.
- When only a speed range is provided, the lowest speed is used for non-injurious tests and the highest for the injurious tests (Allsop et al. 1988). These tests were used for injury assessment as censored data. They were represented as a force range for force comparisons.
- Small impactors below 1 in (25.4 mm) diameter from Hodgson et al. (1970, 1971, 1973) which would be unlikely to be representative of drones were removed. The exception was the 5/16 in (8mm) from Hodgson et al. (1970) which was kept to compare with Mao et al. (2013). It was also used for injury assessment and force comparisons as it was in the simulation database (5 cases), but its removal will be considered in the future.
- PMHS for which a skull abnormality was reported were excluded (only one case in Nusholtz et al., 1984)
- Only vault fractures resulting from a direct contact (comminuted depressed and linear fracture as described in Melvin & Evans, 1971) have been studied. A fracture from the base of the skull was removed as it involves a different injury mechanism (Alem et al., 1984).

For comparison purpose, the conditions used in past validation study of the GHBMC were repeated even if they did not match the criteria on inclusion. This is the case for Hodgson et al. comparison with Mao et al. (2013) who used a 5/16 in (8mm) radius impactor

(already mentioned) and of the injurious woodblock tests of Stark et al. (2019).

CT-scans were only performed in two of the studies (Raymond et al., 2009, Stark et al., 2019). Their authors agreed to share the imaging for this work. Subject specific models were built for three PMHS of Stark et al. (2019) tested with the woodblock or two drones and all seven PMHS of Raymond et al. (2009).

The complete simulation matrix is provided in APPENDIX A with a summary in Table 1. The combination corresponds to a total of 218 test cases. It covers a wide range of velocities, impactor shapes and surfaces, and five impact locations on the head. The 156 tests selected for the injury analysis were run both with and without element failure enabled.

Table 1. Literature data used for the simulations. + denote the references used in the GHBMC validation. * Denote the references in subject specific simulations. The last columns indicate the use of the data. Changes in the number of fractures (e.g. 7/7 for biofidelity and 0/7 for injury assessment) indicate that different tests were used. Biofidelity includes only the tests that have been previously reproduced in simulations (Mao et al., 2013 or Lyu et al., 2022). Number of fractures / number of tests (e.g. 0/7 means 0 fracture over 7 tests).

Study	Impactor type	Impact location & speed	# fractures / # tests		
			Biofidelity	Injury assessment	Peak force comparison
Alem et al., 1984	Cylinder, 10kg	Top (H409): 10.4 m/s	-	1/1	1/1
	Rigid cylinder 10kg with Ensolite tip (0.5-5.1cm)	Top: 6.9 – 10.9 m/s Front: 7.7 – 10.9 m/s	-	0/18	0/18
Allsop et al., 1988+	Semi-cylinder, 14.5kg	Front: 3 – 4.2 m/s	13/13	13/13	13/13
Allsop et al., 1991+	Plate, 12kg	45° lateral: 4.3 m/s	11/11	11/11	11/11
	Cylinder, 10.6kg	Parietal: 2.7 m/s	20/20	20/20	20/20
Got et al., 1978	Head on rigid flat	Lateral: 6.00 – 7.00 m/s	-	2/2	2/2
	Body fall (head) on padded (EPS) flat	Front: 7.67 m/s Lateral: 7.67 m/s	-	0/9	0/9
Hodgson et al., 1970+	Semi-circular (1’’), 4.54kg	Front: 2.74 – 3.54m/s	7/7	0/7	7/7
	Semi-circular (5/16’’), 4.54kg	Front: 1.58 – 3.54 m/s	5/5	1/5	5/5
Hodgson & Thomas (1971) Hodgson (1973)	Plate	Front: 1.58 – 3.87m/s	-	0/5	6/6
		Side: 1.58 – 4.42m/s	-	0/6	7/7
	Semi-circular (1”, ½”)	Front: 2.23 – 4.15 m/s	-	5/13	22/25
	Hemisphere (radius 3”, 5”, 8”)	Front: 2.87 – 3.51m/s	-	3/11	15/15
McIntosh et al., 1993	Cylinder, 25 – 28kg	Temporal: 2.8 – 6.1 m/s	-	3/6	3/6
	Rigid cylinder 25kg, Ensolite tip (2.5cm)	Temporal: 2.9 – 5.9 m/s	-	0/5	0/5
Nusholtz et al., 1984	Rigid cylinder 25-65kg, Ensolite tip (0.5-2.5cm)	Front: 3.8 – 5.7 m/s	-	1/5	1/5
Raymond et al., 2009*	Cylinder, 0.103kg	Lateral: 16.3 – 23.4 m/s	-	2/7	2/7
		Lateral: 31.9 – 35.1 m/s	-	5/7	5/7
Stark et al., 2019*	Woodblock, 1.27kg	Lateral: 5.7 m/s	-	0/1	-
	Drone DJI Mavic Pro, 0.73kg	58° front: 21.3 m/s	-	0/1	-
	Drone DJI Phantom 3, 1.20kg	58° front: 21.4 – 21.9 m/s 58° Lateral: 21.9 m/s	-	0/3	-
Yoganandan et al., 1995+	Anvil	Top: 7.2 – 8.0 m/s 45° front: 7.1 m/s 35° rear: 7.3 m/s	6/6	-	6/6
Total			62/62	67/156	126/175

Head model

The GHBMC 50th percentile male detailed occupant version 6.0 was used for all simulations (GHBMC M50-O v6.0) with the LS-Dyna solver (R13.0 single precision, Ansys). The head model was developed by Wayne State University (Mao et al., 2013) and has been validated against different impact conditions to demonstrate its bio-fidelity (Mao et al., 2013, Lyu et al., 2022). Its geometry is based on a subject with an anthropometry close to the 50th percentile male (Gayzik et al., 2011). The mesh of the skull describes separately the inner and outer tables (cortical bone) and the diploe in between (cancellous bone). The diploe is modeled with one layer of solid elements while the inner and outer tables are modeled with one layer of solid elements covered by a layer of 1mm thick shell elements using the same material properties (Figure 1). This means that cortical bone properties are represented twice within half of cortical shell thickness: once by the shell and once by the solid. The reason is not explicit. It may be related to the description of the bending mode as all solid elements use a single integration point formulation. The shell is fully integrated. The bone, composed of three layers of solid, is covered by a scalp and a skin shell. The skull and scalp are rigidly attached (coincident nodes). All other structures of the head (brain, face, etc.) were kept for the simulation. The mass of the head is 4.67 kg.

While the mesh of skull did not seem to change over the years, its mechanical properties have evolved as publicly documented in Mao et al., 2013 (model version 4) and Lyu et al., 2022 (model version just prior to version 6). For both studies, the skull properties are the same in all regions and all derived from the literature. The inner and outer tables have a modulus of 15 GPa derived from Wood (1971) and the diploe a modulus of 0.6 GPa derived from Melvin & Evans (1971). In version 6.0, the tables have a first principal strain-based failure and element erosion at 0.88% (Lyu et al., 2022) while it was 0.42% in early versions (Mao et al., 2013). The diploe has a maximum principal stress-based failure and element erosion at 20MPa. For this study, the skull was considered fractured if at least one element was eroded. Simulations were also run without erosion for the work on a probabilistic criterion (presented later in the Post processing section of the Materials & methods).

The skin and scalp properties have also evolved over the years, with the temporal scalp properties differing from the rest of the scalp in recent versions and parameters of the viscoelastic material law changing as well. For the current study, the baseline model was modified to remove a void/gap present in the original mesh between the scalp and the skull near the zygomatic arch which prevented the normal load transfer to the bone in temporal impacts. The gap was filled by moving the scalp nodes closer to the skull and adding a filler with one-point nodal pressure tetrahedral elements (formulation 13) with the same properties as the scalp (Figure 2). A watertight boundary is maintained between the filler and the original scalp.

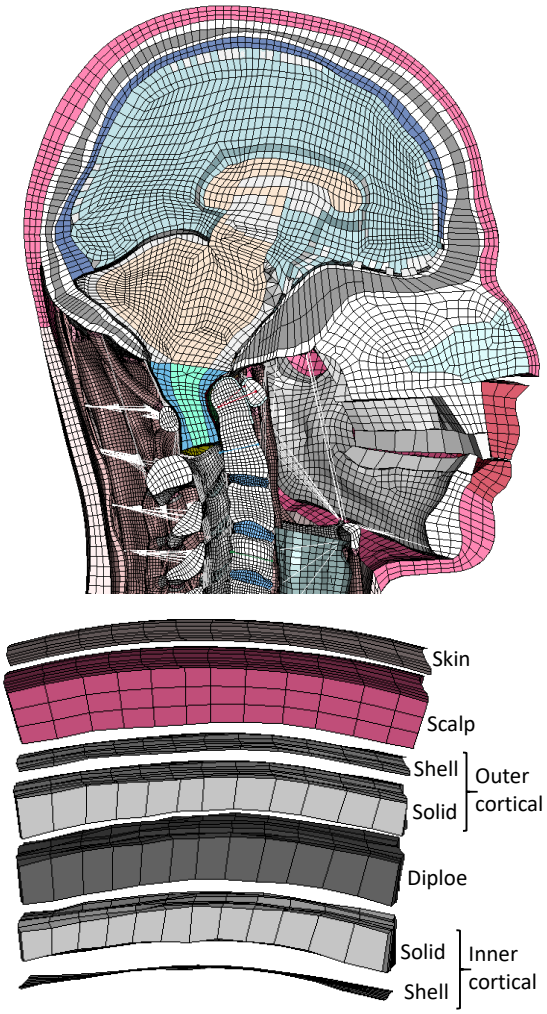

Figure 1. GHBMC head model cut (top) and skull structure (bottom). Each of the five bony parts (inner or outer cortical shell or solid, diploe) has between 11,000 and 12,000 elements.

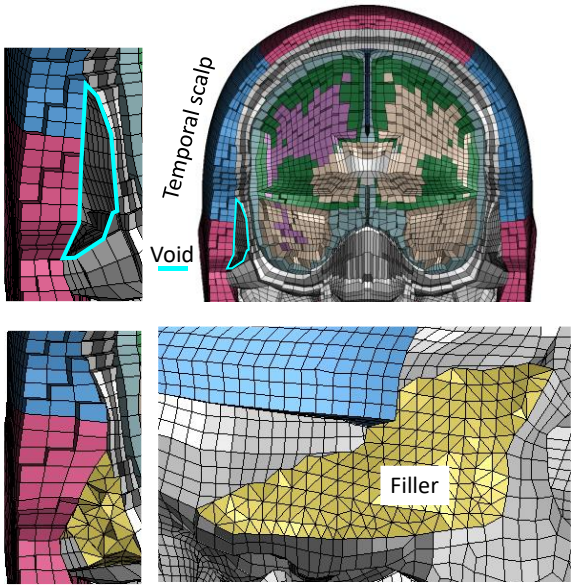

Figure 2. Scalp modelling with a representation of the temporal scalp and the void/gap in the baseline mesh (top). The internal surface of the scalp mesh was moved, and a tetrahedral filler was added. Tied contacts were also added where necessary.

Subject specific modelling

The GHBMC head was morphed to the geometry of ten PMHS using their CT-scans. The process included multiple steps. First, a surface mesh of the skull and neck (reference model) is registered to the shape of the GHBMC skull and neck using the Anatoreg software package (AnatoScope SA, Montpellier, France). The deformable registration is initiated by a landmark-to-landmark registration (rough transformation) followed by a more detailed surface-to-surface registration using a grid-based algorithm (Gilles et al., 2010). Then, a rough segmentation of the skull (for Raymond et al., 2009) and the skull and neck (for Stark et al., 2019) was performed for each PMHS by thresholding and region growth in 3DSlicer (v5.6.1, www.slicer.org, Fedorov et al., 2012). The reference mesh was registered onto this segmentation using Anatoreg again. Finally, all vertices of the reference mesh are used as control points (source: GHBMC registration; target: PMHS registration) to morph the finite element model using the RBFInterpolator function of the Python SciPy package (v1.11.4) with the smoothing option set to 1000. More details are provided Figure 3. The segmentation included the skull, mandible and for, Stark et al. (2019), the cervical spine vertebrae. The cervical spine was kept as it (with the curvature from the CT-scan) and not repositioned to the subject specific test position. For the skull, a first attempt to separate the three bone layers (inner and outer table, diploë) was unsuccessful (very noisy data) due to the insufficient CT-scans resolutions for that purpose. Therefore, for now, the segmentation was only performed on the external shapes of the skull.

For Raymond, as the CT-scans were performed after the tests, the side of the skull without fracture was symmetrized. For the one PMHS skull that sustained fractures on both sides, the side with the smallest fracture was used with some manual corrections to prevent discontinuities.

Raymond et al. (2009) observed that for their impact condition, the subject-to-subject variation of scalp thickness at the impact site could be related to the fracture occurrence. To explore this issue and try to see if the same tendency could be observed in simulations, the soft tissue thickness was adjusted only for that setup using the measurements provided in the study. The soft tissues are morphed along with the skull. While this can provide a reasonable scalp target as the morphing accounts for size and shape changes, it does not account for variations of scalp thickness between PMHS. Raymond et al. (2009) measured scalp thickness on the left and right side of each PMHS (between 5 and 16 mm, average 8.1 ± 3.3 mm) and suggested that the differences of scalp thickness between PMHS may be important for injury. Therefore, for that test condition, the scalp thickness was adjusted at the impact site to represent these variations. On the model, a thickness of 13.1mm was measured at the center of the impact site but the thickness varies considerably in that region. As it is unclear how the correspondence could be established between that measurement and Raymond's measurements, the difference of thickness between each PMHS and the 8.1 mm average was chosen as the model thickness target. For example, for a PMHS with reported left scalp thickness of 6 mm (2.1 mm below from the PMHS average), a target of 11mm was selected for the model (2.1 mm below the baseline model). For the implementation, the skin surface near the impactor was offset and mesh locally smoothed iteratively until the error on the measurement was about 1mm at most. Examples of surfaces for the extreme cases are shown in Figure 4.

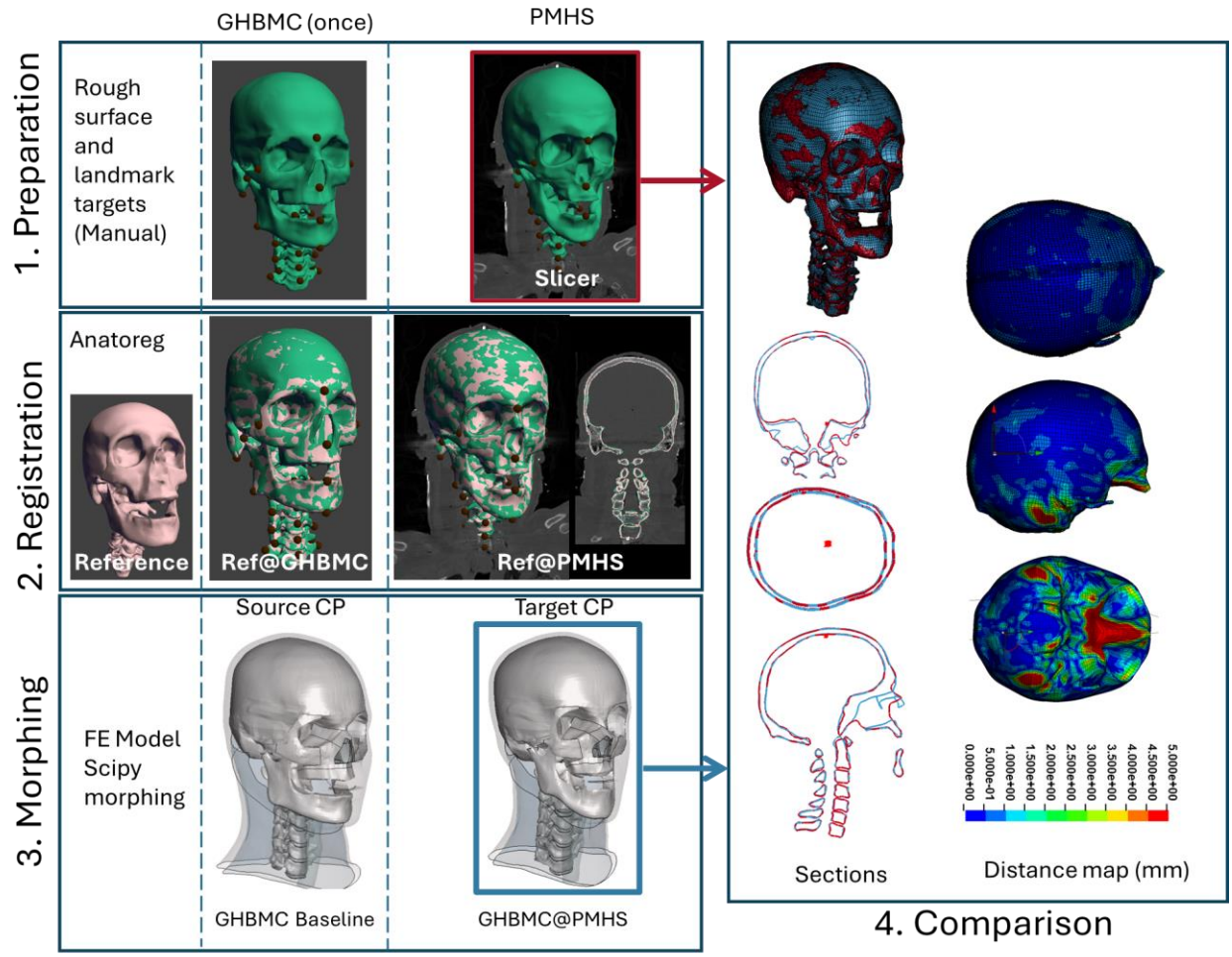

Figure 3. Illustration of the process to generate subject specific models. A reference mesh is registered (2) onto target surfaces derived from the GHBMC model or the PMHS CT-scan (1). The process is checked against CT-scan for the PMHS (2). The vertices of registered meshes are then used as control points to transform the baseline FE model (3). The resulting model is close to the PMHS surface (typically within less than one millimeter) except on the base of the skull and the face (which are not regions of interest for this study) for which the difference can be larger (4).

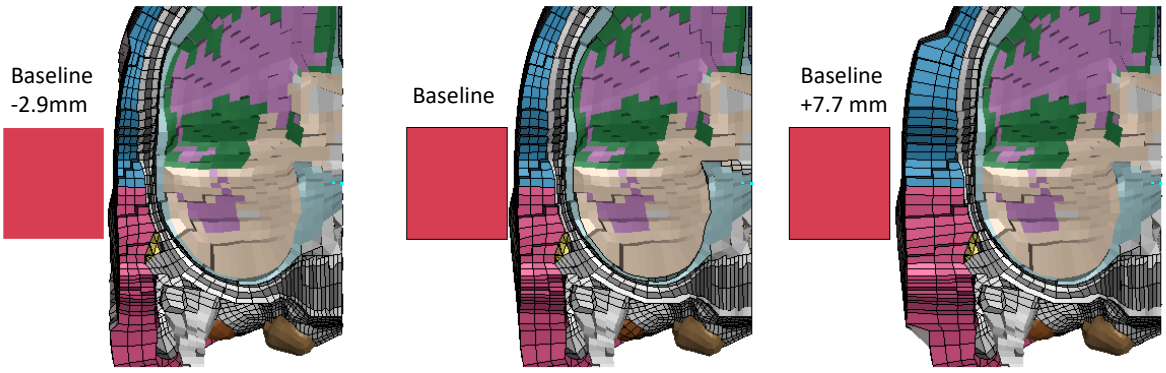

Figure 4. Adjustment of the scalp thickness in the case of Raymond et al. (2009) subject specific models. The baseline thickness (center) was adjusted to represent PMHS variations. The extremes are shown: a 2.9mm reduction (left) and a 7.7mm increase (right).

Position, material and numerical sensitivity

To check for possible interactions between the subject specific geometry (vs. baseline) and the impact position, small sensitivity analyses were conducted for the two studies for which subject specific geometries were used (Stark et al., 2019, Raymond et al., 2009). For Stark, the drones and woodblock were either positioned in the nominal configuration (e.g. 58 degrees, symmetrical) or their position adjusted based on the video data. For Raymond, as no video data were available, small shifts (±10 mm) of the impact location along the anteroposterior or inferior superior axes were performed.

Sensitivity analyses were then conducted on the scalp and the bone numerical formulations as they are potentially of interest considering the application. The scalp properties have evolved with the versions of the GHBMC (Mao et al., 2013, Lyu et al., 2022) and include a separation between temporal properties and properties in other locations which would seem difficult to justify by anatomical differences. Considering the possible importance of the scalp for injury based on Raymond et al. (2009) analysis, the following scalp properties were tested in Raymond's setup:

- Homogenous properties corresponding to either the temporal or the remainder of the scalp of the GHBMC v6.0
- Previous versions of the GHBMC material properties as provided by Mao et al., (2013), Lyu et al., (2022)
- Publicly available properties from the literature (KTH model, Lindgren et al., 2024) or open-source models (PIPER child, Beillas et al., 2016 and Viva+, John et al., 2022).

For the skull, the presence of both shells and solids in the same location may lead to an overestimation of the skull thickness in the subject specific models. Also, the single integration point solids may not describe well some of the bending modes (e.g. for the diploe). The shell was removed, and fully integrated elements tested in Raymond's setup.

Boundary and simulation conditions

All impactors called rigid in the reference studies were modelled with rigid bodies. Although the wood block used in Stark et al. (2019) could be considered rigid, it was simulated as a deformable object using a wood material as Stark et al. (2019) did in their simulations (MAT_WOOD_PINE).

For deformable impactors, simplified models of the two drones selected for Stark et al. (DJI Mavic Pro and DJI Phantom 3) were developed (details in APPENDIX B). The goal was to be able to load the skull as in PMHS tests. The drones main components were surface scanned, meshed and assembled. Their properties were adjusted until the gross kinematics and reaction force approached those of a physical test against a rigid object. The drone models were then checked against dummy tests before being used against the human model. For the padding, samples of EPS and Ensolite were tested at low speed on a material testing machine. Curves derived from these tests and literature were used in MAT_LOW_DENSITY_FOAM. The process is detailed in APPENDIX B.

For Allsop et al. (1988, 1991), Raymond et al. (2009) and Yoganandan et al. (1995), only the head was kept as in the tests. The head and neck were used for other tests, with the neck having a free boundary condition. Full body preliminary simulations showed that the effect of keeping only the neck with free boundary conditions was small (less than 6% on the force, APPENDIX D) compared to full body simulations (Got et al., 1978 full body drop tests, Alem et al., 1984 longer duration padded tests). The differences were highest for the axial neck loading.

For the tests in which the skull was fixed inside a plaster (Allsop et al. 1988, 1991, Yoganandan et al., 1995), only the nodes of the skin within the plaster were fixed. Impact parameters and positions were set as described in the original studies. When pictures or drawing of specific tests were present in the publication, a visual check was used to verify the conditions. For Stark et al. and Got et al. polystyrene tests, the test laboratories shared their original data and movies could be used.

The initial velocity was applied to the impactor except for Yoganandan et al. tests for which a constant speed was used. When known, exact velocities were used for each test. The contact between impactor and skin was modeled using an automatic surface to surface contact with a SOFT=2 option. In case of numerical issues (negative volume in the scalp, penetrations), a single surface contact with edge-to-edge treatment and sometimes internal contact treatment was used. The elapsed time of each simulation was only a few minutes on a 48 cores machine equipped with AMD EPYC 7F72.

Post processing

When not specified in the articles, impactor forces were saved at 100 kHz. For others, the sampling rates

of the studies were used. For example, Allsop et al. (1988) and Allsop et al. (1991) impactor forces were saved at 20kHz and 5kHz, respectively. Element strains were extracted from animations sampled at 20kHz. For the analysis of the response / biofidelity, the experimental curves were digitized except for Stark et al. (2019) for which numerical data was provided by the authors. As they were available in most studies, experimental peak forces were compared to the simulations. In the simulations of Yoganandan et al. (1995) tests, the stiffness is computed as the slope of the linear portion of the force-displacement curve (with bounds selected manually). The head acceleration was generally not analyzed because (1) some of the tests were performed on a fixed head which would limit the scope of the comparisons (2) due to the very brief contact durations in some cases, large vibrations and variations of the acceleration magnitude are expected and these would make the analysis difficult and dependent on the instrumentation (e.g. precise location). The skull acceleration was only analyzed for Stark et al. (2019) because (1) force was not measured and (2) full details about the tests facilitate the comparison (subject specific geometry, exact instrumentation location, videos, etc.). A simplified method was used for the analysis: instead of defining every sensor of the 6aω accelerometer mount, a constrained interpolation based on a skull portion near the base of Stark 6aω tetrahedron was used to compute the acceleration at the CG of the head. Its components were filtered using a SAE CFC 1000 before computing the resultant.

Regarding injury prediction, all simulations were run twice:

- A first time with failure/erosion enabled: the occurrence of element erosion within the diploe or tables were captured, and fracture was associated with the failure/erosion of at least one element. Element failure was compared to the fracture status and the sensitivity and specificity computed.

- A second time without erosion: the three Green St Venant principal strains were exported for the diploe, and solid and shell parts of the tables. Principal strains are ranked by amplitude in LS-Dyna and the first principal is typically in tension, the third in compression and the second is related to shear. Percentiles of those strains as well as the levels reached by the top 1 (maximum), 2, 5, 10 etc. elements were computed. These metrics were used to compute risk curves using as a guideline the ISO/TS 18506:2014 procedure that was also detailed in (Petitjean et al., 2012). To summarize, all points were considered censored. The best distribution was selected based on the Akaike Information Criterion. A risk ratio (RR) was computed as the width of the confidence interval divided by the mean level of the criterion. Because it is a ratio of strains (or forces), it is independent of the magnitude of the criterion. A rating was associated to this ratio (good below 0.5, fair between 0.5 and 1, marginal between 1 and 1.5, unacceptable above). All computations were done in R (R Core Team, 2018) using the scripts provided with the ISO/TS modified to add additional outputs. To summarize, risk curves are built using survival analysis and different distributions (loglog, lognormal, Weibull). The Akaike Information Criterion is calculated and the best distribution (i.e. with the lower AIC) is kept. The confidence interval is built and the quality index (ratio between the width of the confidence interval and the value) is calculated. The procedure is automated and applied systematically to all parts and strains independently of potential loading mechanisms (the strains are considered as numerical predictors).

In both cases, to prevent any issue with artefactual fractures/erosion in regions that would not be of interest for the analysis, the face, the base of the skull and the inferior regions of the temporal (inferior to the zygomatic arches), and occipital bone (inferior to the occipital protuberance) were removed.

RESULTS

Model response / biofidelity: comparison with previous validation studies

Illustrations of the test setups and deformations at peak load or fracture are shown in Figure 5 for Allsop et al. (1988, 1991, used in Lyu et al. 2022), Hodgson et al. (1970, used in Mao et al. 2013), and Yoganandan et al. (1995, used in both).

Force-deflection curves of Allsop et al., (1988, 1991) are compared to the simulations in Figure 6. All tests were injurious, and element failure occurred in every simulation. Current responses follow the overall trend of Lyu et al.: the parietal and temporal responses are within the experimental range while the frontal responses are stiffer and reach much higher failure forces. However, in all three setups, the peak/failure forces are higher with the current model than Lyu's version. The reason for this discrepancy is unknown

but it seems significant as setting the cortical bone erosion to 0.42 % (i.e. the value used before Lyu) makes the peak forces much closer to Lyu's version.

For Yoganandan et al., (1995, all fractured tests), only peak forces were compared by Mao et al. (2013) and only stiffnesses were compared by Lyu et al. (2022) (because these are the metrics used respectively in the two studies). Both are provided in Table 2. Similarly to Allsop's setup, the peak forces were higher for the current model (19.8 kN) than the experiment or Mao (11.9 and 11.6 kN, respectively). The stiffness (3.7kN/mm) is close to both experiments and Lyu (4.0 kN/mm). Running simulations with the 0.42% erosion limit used in Mao's version decreases the peak force to 16.7 kN in average, still above experiments and Mao. This suggests that other factors besides the bone failure strain affected the model peak forces. These could include skull or scalp material properties or their thickness for example.

Peak forces for the Hodgson et al. (1970) setups are summarized in Table 3. The trend is consistent with the previous observations, i.e. the force predicted with the current model is higher than in the experiment or the previous versions. Mao et al. (2013) lower failure limit of 0.42% may partially explain these differences (cf. Table 2).

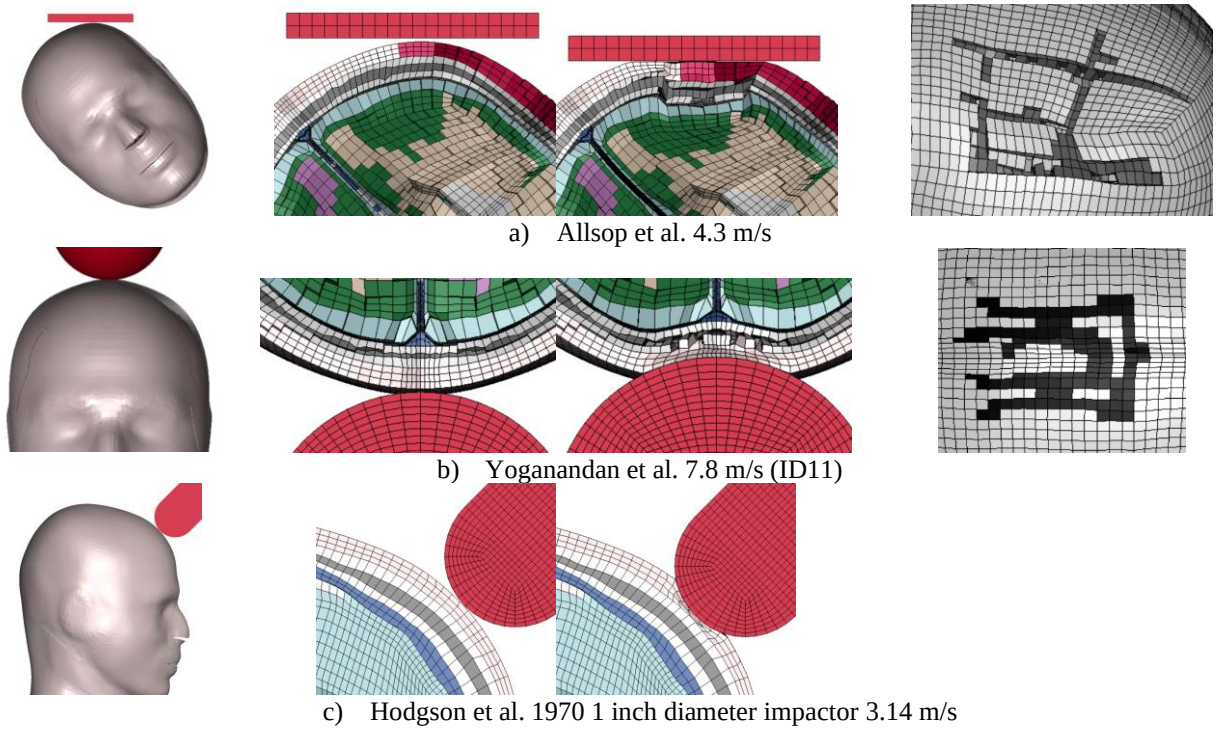

a) Allsop et al. 4.3 m/s

b) Yoganandan et al. 7.8 m/s (ID11)

c) Hodgson et al. 1970 1 inch diameter impactor 3.14 m/s

Figure 5. Comparison with past simulation studies from Mao et al. (2013) and Lyu et al. (2022). Illustration of the tests setup (left), local loading (before contact and at peak, middle) and failure (when occurring, right).

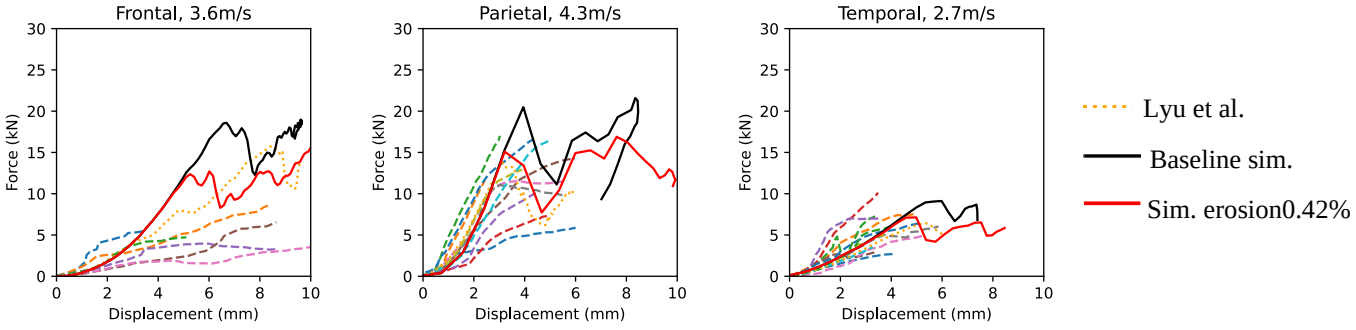

Figure 6. Force-deflection responses in frontal impacts (Allsop et al., 1988), parietal and temporal impacts (Allsop et al., 1991). Experimental curves are in dashed lines, simulation curves from the current study in solid lines and Lyu reported model response in dotted lines. Baseline simulations use failure/erosion at 0.88%, "erosion0.42%" at 0.42%. The drops correspond to element failure that propagates.

Table 2. Stiffness and first peak force in the Yoganandan et al. (1995) setup. The simulations (sim) include results obtained for the current study (version 6.0), peak forces from Mao et al. (2013, version 4 of the model) et Lyu et al. (2022, version just before 6.0). Simulations with the 0.42% failure strain used in Mao et al. were run for comparison. The experimental forces are denoted by exp.

ID	Impact	Speed (m/s)	Peak force (kN)				Stiffness (kN/mm)		
			Exp	Mao	Sim	Sim 0.42%	Exp	Lyu	Simulations
7	Vertex	7.2	14.0	10.6	19.6	16.8	4.8	4.1	3.5
8	45° frontal	7.1	13.6	13.7	19.6	16.6	5.9	4.8	3.6
9	Vertex	7.6	13.6	10.7	19.3	16.6	2.5	4.2	3.8
10	35° rear	7.3	10.0	11.9	20.7	16.4	2.5	2.5	3.7
11	Vertex	7.8	8.8	11.5	19.8	16.9	4.1	-	3.8
12	Vertex	8.0	11.6	11.5	19.6	16.8	4.4	4.3	3.8
	Average		11.9	11.6	19.8	16.7	4.0	4.0	3.7

Table 3. Peak force in the Hodgson et al. (1970) setup. The simulations include results obtained for the current study (version 6.0) and Mao et al. (2013, version 4 of the model).

Test number	Impactor radius	Velocity (m/s)	Peak force (kN)		
			Experiments	Mao	Simulations
1504, 1536, 1582, 1589, 1615	1 in	2.74	5.9 ± 1.1	7.2	12.1
1486	5/16 in	3.14	5.9	8.6	14.2
1581	5/16 in	3.54	4.2	9.4	16.5

Raymond et al. (2009) rigid high velocity tests

Baseline and subject specific models

The baseline responses and effect of subject specific modelling can be seen in Figure 7 and Figure 8. As for previous setups, the forces predicted by the model were much higher than in the experiments. For condition A (n=7), the mean ± SD peak forces were 3.7 ± 1.2kN, 8.2 ± 1.1 kN and 7.4 ± 1.7 kN for experimental tests, baseline simulations and simulations with subject specific geometry, respectively. Corresponding values for condition B (n=7) were 5.8 ± 1.9 kN, 13.4 ± 0.5 kN and 13.3 ± 1.4 kN.

The effect of the subject specific geometry on the peak force was limited as seen on the average. It did not explain the discrepancy between response and baseline models, and it was not statistically significant (p=0.26, Wilcoxon signed rank test). It only increased the variance (standard deviation) as it could be expected. The number of failed elements varied with the force: it increased in some cases (e.g. PMHS 2427, PMHS 2965) and decreased in others (e.g. PMHS 2426 and 2978). The peak force decrease for PMHS 2939 was attributed to the large scalp thickness of the PMHS (about 15mm vs between 5 and 8 mm for all others).

The tests resulted in skull fractures in two out of seven PMHS (condition A) and five out of seven tests (condition B). For the baseline models, some elements (shells or solids) failed in four condition A and all seven condition B. If considering only the outer cortical solid element, no failure was observed in condition A, while failure was observed in all the baseline simulations in condition B. With subject specific models, outer cortical solid elements failed in one condition A and six condition B. The change was in part due to subject specific model 2939 with the increased scalp thickness that did not fail while the baseline model did. This is in line with Raymond et al. observation on the importance of the scalp.

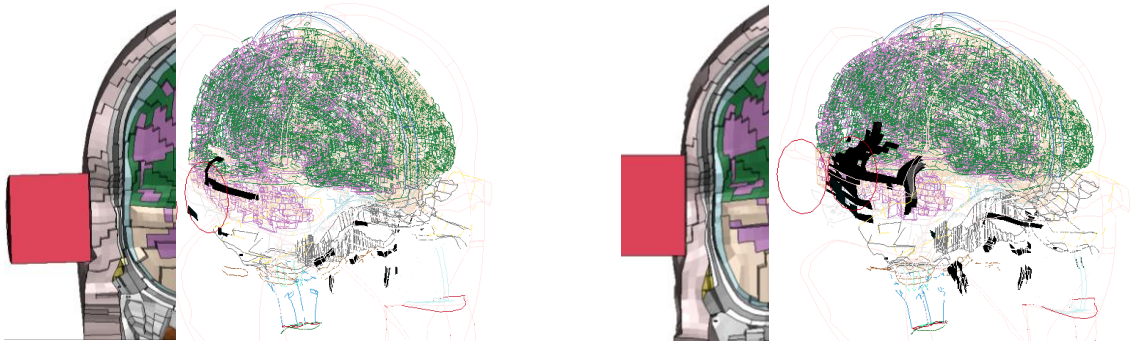

Baseline Subject specific

Condition A: 23.4m/s to the right side of the skull

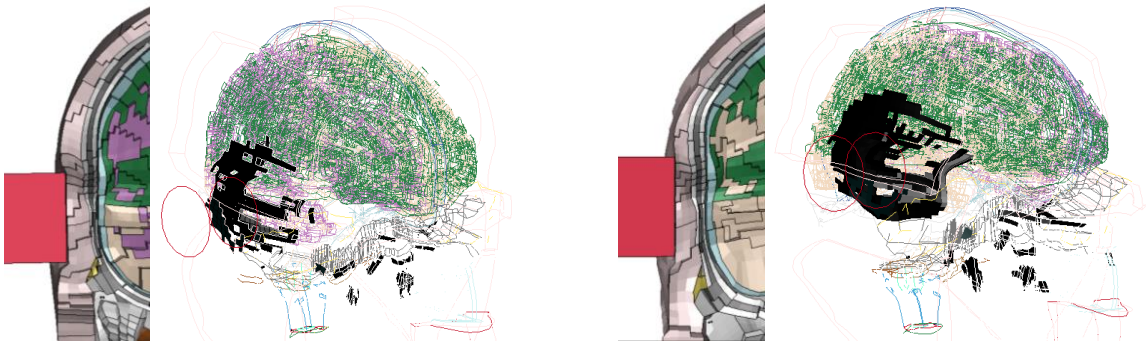

Baseline Subject specific

Condition B (34.2 m/s) to the left side of the skull (shown on the right to facilitate comparisons)

Figure 7. Peak compression and failure patterns for PMHS 2427 of Raymond et al. (2009). All peaks were within 0.5 ms of contact. Elements that failed away from the impacted region (face and base of the skull) were not considered in the analyses.

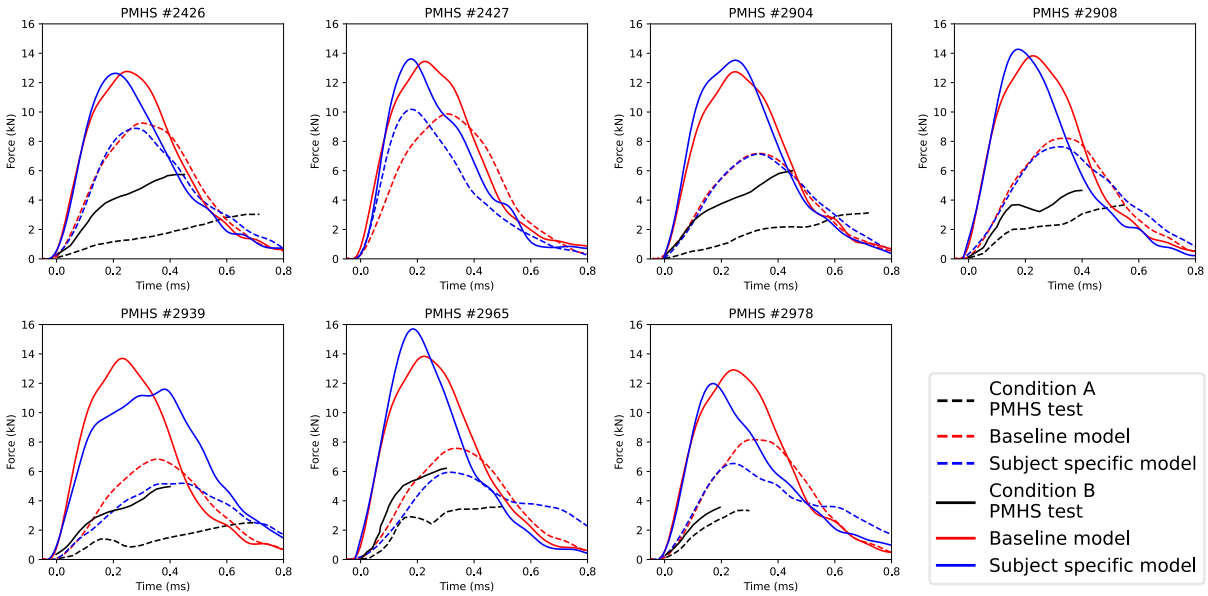

Figure 8. Force-time curve in Raymond et al. (2009) tests (black lines), simulations with baseline model (red lines) and simulations with the subject specific models (blue lines). Condition A in dashed lines, condition B in solid lines. The experimental curve of 2427 was not available.

Sensitivity

Small shifts (±10 mm) of the impact location along the anteroposterior or inferior superior axes resulted in substantial changes of peak force (from 12.5 kN to 17.8 kN, Figure 9) and that were more pronounced for the subject specific than the baseline model. For most PMHS, the subject specific temporal shapes are more curved than the baseline, which could affect the contact non-linearity and scalp engagement. Furthermore, the lateral impact location in Raymond et al., 2009 (aligned with the center of gravity, also used by Allsop et al., 1991, and Stark et al., 2019) is overlapping the two scalp parts (temporal, remainder). Small variations of positions therefore engage different material properties of the scalp.

The effect of the scalp material properties on the response was then examined. The force time histories (Figure 10) vary considerably with the material properties, including between versions of the GHBMC. The simulated forces are almost always higher than the experimental ones and, at high speed, the peak forces vary by a factor of almost 3 (between 7.6 kN and 19.6 kN). The hyperelastic properties used in PIPER child model led to the highest forces, followed by various versions of the GHBMC, Lindgren (KTH model) and Viva+. The scalp properties of the oldest version of the GHBMC (v4.1) are the only ones leading to forces close to the experimental responses at both velocities. The scalp properties also affect the number of elements failing in the skull (e.g. 67 with the GHBMC v4.1 scalp, 546 for the GHBMC v6.0 baseline, same patterns).

Finally, the effect of the bone element formulation was checked. As previously explained, the superimposition of shells and solid doubles the material on the skull surfaces, which may be an issue for subject specific models whose geometry matches the ones of the PMHS. After removing the shell and switching the solids to a full integration, the peak force was greatly reduced at high speed/most injurious condition: it went from 13.8 to 11.2 kN for the baseline, and 15.7 to 11.6 kN for the subject specific model. The effect was much less marked for the lower speed (e.g. 7.6 to 6.6kN for baseline model). The failure patterns are similar for the two formulations, but the number of failed elements is higher in the 3D only case. Altogether, this could indicate that the formulation change affects the failure and its propagation more than the stiffness through the change of thickness.

Stark tests with woodblock and drones

The acceleration at the head center of gravity (CG) transferred from a mount positioned on the PMHS skull was used for the comparisons with the CG acceleration estimated using a constrained interpolation in the model. As the high frequency large vibrations observed on the model acceleration would prevent comparisons, a SAE CFC 1000 was applied to all signals in the same way the HIC is computed (components are filtered first). The effect on the experimental curves was limited, suggesting that the damping may be lower in the simulation than in the test or that the difference of methodology for the calculation (filtering) affects the result.

All woodblock tests (the second being injurious) were simulated with both baseline and subject specific models (Figure 12). The geometrical effects are limited, but the peak values are closer with the subject specific model, and the overall experimental acceleration shapes are described at 5.7 and 9.2 m/s. More substantial differences are visible at 12 m/s.

For the drones, the baseline model was run with the baseline drone position (nominal angles) followed by the subject specific model first with the baseline drone position and finally with the drone position adjusted based on the test videos. Impact positions and engagement of drone structures are illustrated in Figure 13 with acceleration results summarized in Figure 14. The subject specific geometry with the adjusted drone position improved substantially the match between simulation and test in all five cases. The improvement seems more due to the adjustment of the impact position than the subject specificity (PMHS 7677). It suggests that the responses could be very sensitive to the contact nonlinearity and drone structure engagement, which is itself affected by the drone position and by the PMHS geometry.

Simulations with deformable impactors

The results of the simulations with padding followed the overall trends observed with rigid impactors, i.e. a tendency to overestimate the peak force. As no failure or fracture were observed in most of the padded tests, the failure mechanism does not play a role here. The trends are the same for the two types of padding (Ensolite and EPS), suggesting that both padding models have the same issues or that the response of the human model is involved. Illustrations in setups from Got et al. (1978) and Nusholtz et al. (1984) are provided in Figure 15. The relative lack of compression of the scalp is visible on both setups. This may be due to large contact surface and the relative incompressibility of the tissue or the material model. Similar conclusions can be made from the simulations of McIntosh et al. (1993) lateral tests with Ensolite padding: no fracture was observed in the tests nor in the simulations, and the tendency of the model to overestimate the peak force.

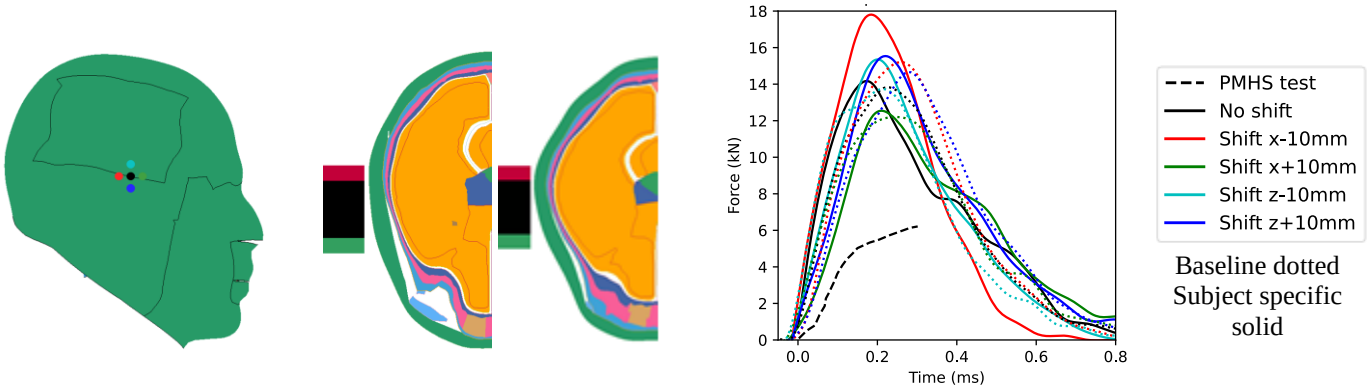

a) Impactor center (left) and width in an horizontal section on baseline (center) and 2965 model (right)

b) Response for the test 2965R at 35.2m/s

Figure 9. Influence of a 10mm shift of impact location from the center of gravity on force-time curves. Curves colors correspond to the dots representing the impactor center location (a).

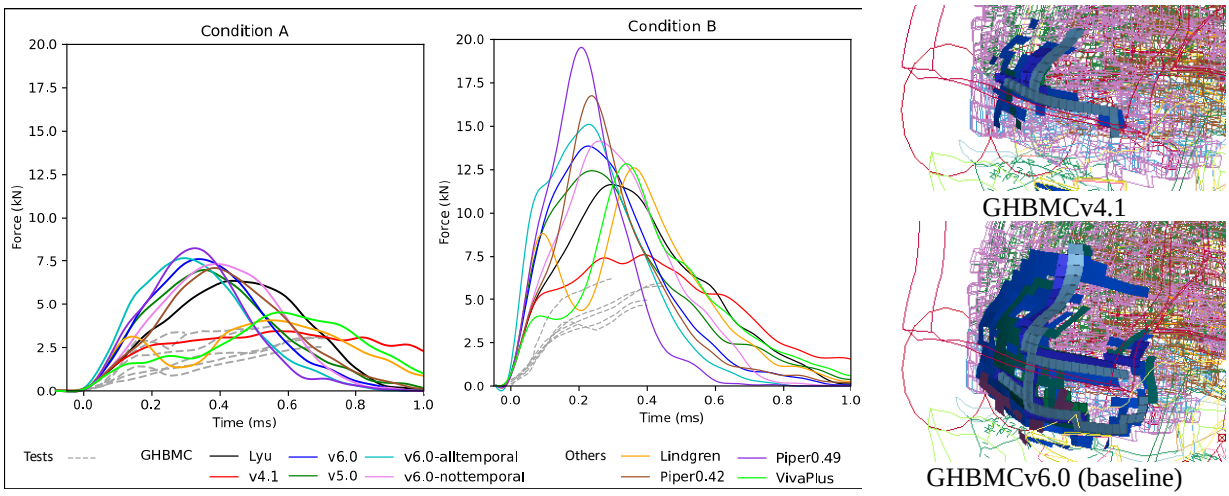

Figure 10. Effect of scalp material properties in Raymond et al. (2009) setup: force time history (left) examples of failure patterns at the highest speed (right). Simulations were run at 18m/s and 35.2 m/s (speeds for the PMHS 2965, i.e. the PMHS with the highest forces). GHBMC properties correspond to different versions of the model. All temporal and not temporal correspond to version 6 of the model with homogenous properties (temporal or not). Other models properties (PIPER, KTH/Lindgren, VivaPlus) were applied to the whole scalp. Failure size and patterns for two scalp properties at 35.2m/s.

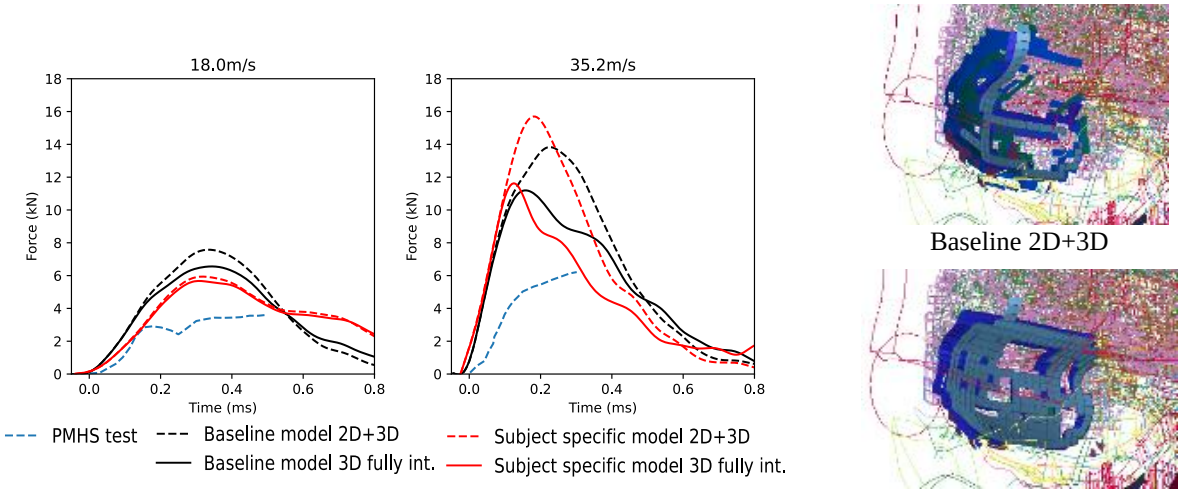

a) Force b) Failure patterns at 35.2m/s

Figure 11. Effect of bone element formulation on the force time history (a) and failure patterns (b) for the PMHS 2965 test conditions. The current formulation (2D over 3D elements) was replaced by 3D fully integrated elements.

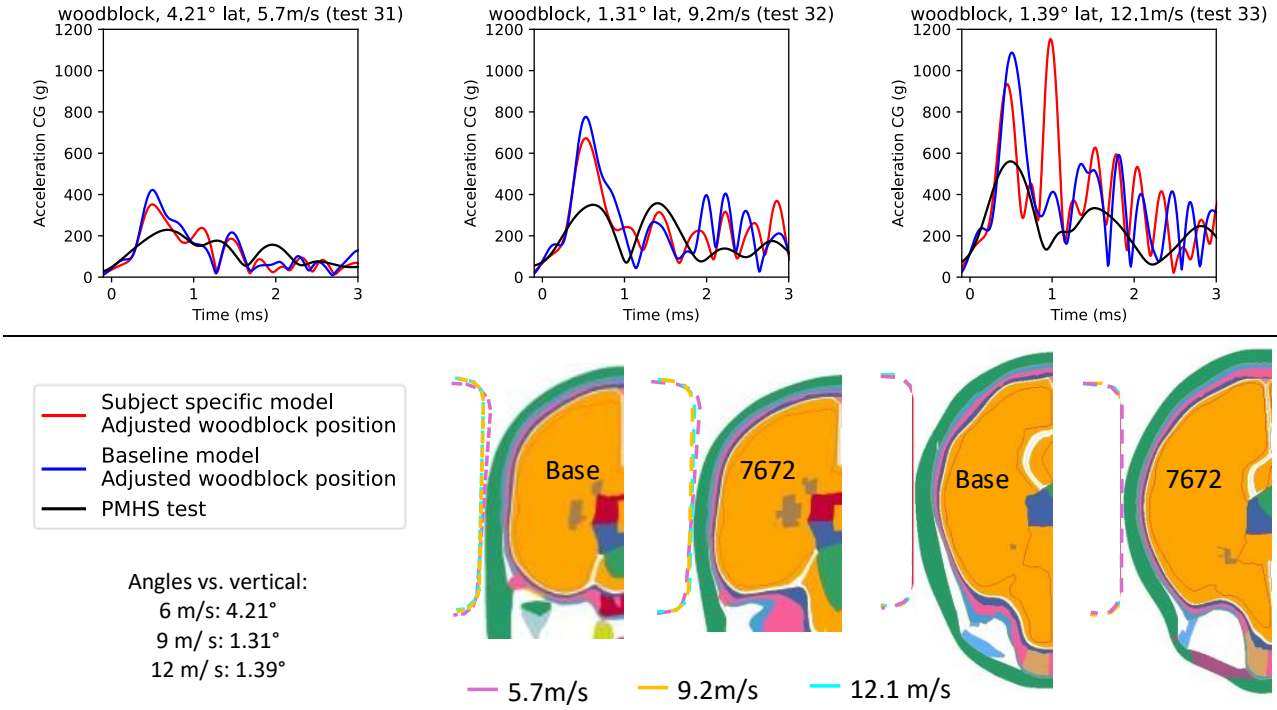

Figure 12. Simulation of Stark woodblock tests. Note that all tests were repeated on the same PMHS and that the second one was injurious. The positions of the woodblock (adjusted from the video) are shown for each model and speed. For both tests and simulations, accelerations are transferred to the head CG from the location of the instrumentation in Stark. All curves are filtered SAE CFC 1000.

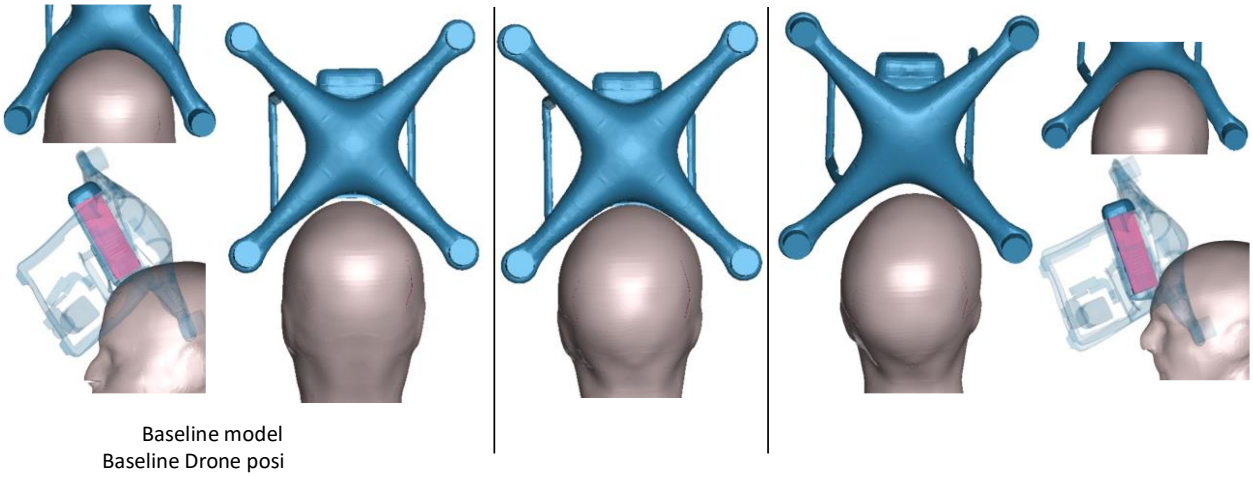

Figure 13. Example of simulation conditions for the Phantom 3 test on PMHS 7677. The baseline model (left) is first impacted using the baseline drone position (58 degrees). Then, the subject specific model is impacted using the baseline drone position (center) and the drone position adjusted based on the videos (right). The engagement of the drone arms and the relative position of the battery with respect to the head are shown for the two extreme cases.

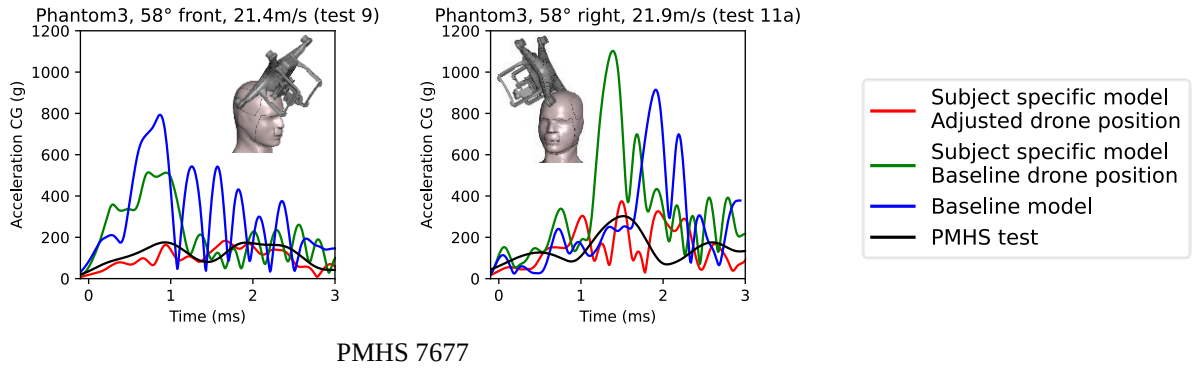

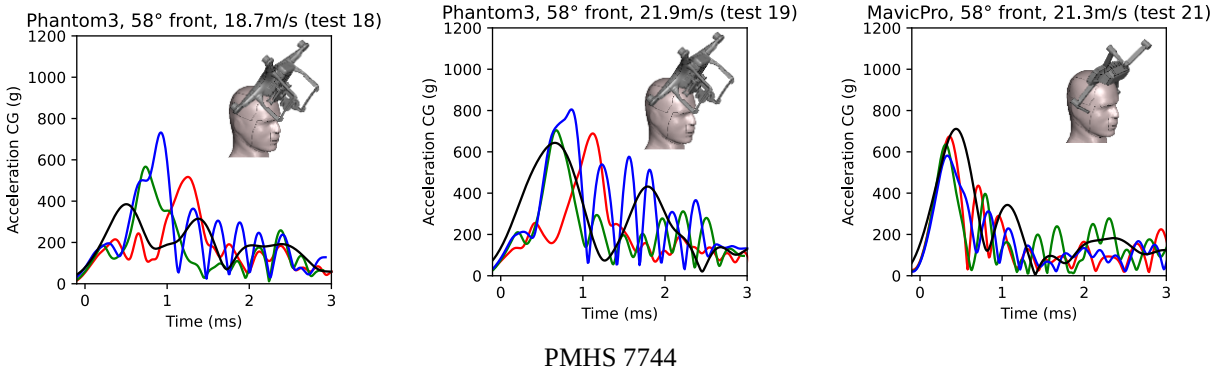

Figure 14. Simulation of five drone tests from Stark et al. (2019). Two drones (Phantom 3 and Mavic Pro) and two PMHS were used. For both tests and simulations, accelerations are transferred to the head CG from the location of the instrumentation in Stark. However, the model uses a constrained interpolation while the experimental data is based on a 6aω tetrahedral mount. All curves are filtered SAE CFC 1000.

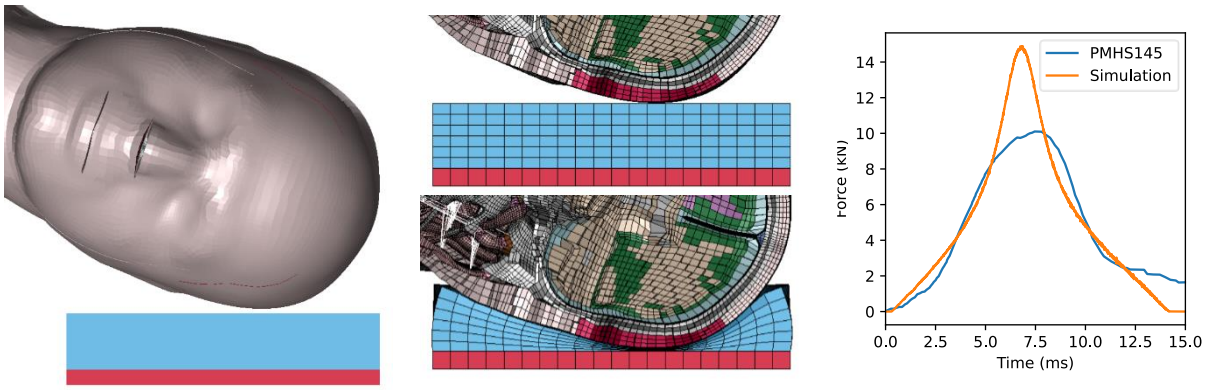

a) Comparison with PMHS 145 from Got et al. (1978) with expanded polystyrene padding.

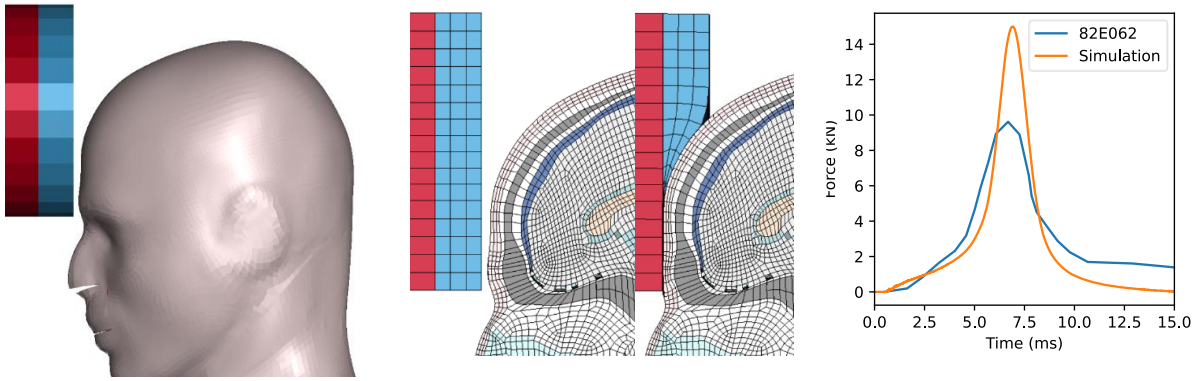

b) Comparison with test 82E62 from Nusholtz et al. (1984) with Ensolite padding.

Figure 15. Examples of simulations with each type of padding material. From left to right: test setup, deformation near peak force and response curves. There was no model failure or PMHS fracture in both cases.

Force and fracture data for all simulations with failure

Experimental peak forces and fracture status were compared to the simulation forces and element failure status. As the time of fracture is typically unknown in experimental studies, the force provided typically corresponds to the peak force and not necessarily to the onset of fracture. For simulations, both peak and failure initiation forces (when the first element is eroded) were calculated to quantify the difference between the two as the element erosion may not represent well the actual propagation of a fracture. Comparisons by study and impactor type are provided in Figure 16 with all numerical values provided in APPENDIX A.

While the ranges of experimental and failure initiation forces are similar for the rigid impacts (e.g. 2.5 to 9.5 kN for Raymond tests), the peak forces are typically much larger in simulations (6.8 to 13.9 kN still for Raymond tests). A similar trend is present for the cases with deformable impactors: while simulation peak forces reach over 30 kN, the failure initiation forces only reach 22 kN, which is this time higher than peak experimental forces (about 17kN at most).

The simulations were overall unable to capture the experimental variations between tests of a study. Several examples and reasons could be provided. Allsop et al. (1991) only have two test conditions, described by one simulation each. These cannot describe the experimental variations within each test condition (e.g. from about 5kN to over 15 kN). These variations may be due to subject-to-subject variability or to small variations of impact conditions (some of which were partially explored in previous sections). This phenomenon is also likely present for other studies such as Hodgson et al. (1971, 1973) for example although it may be partially hidden / confounded with variations of experimental conditions (e.g. change of impact side, variation of velocity).

Therefore, averages of all PMHS per study (separating padded from rigid tests) were computed to try to help identify systematic differences (Figure 17). The results suggest that simulation peak forces are about twice as high as the mean per study, while the failure initiation forces are similar. The results also highlight some

differences between studies that can be difficult to explain. For example, Alem et al. (1984) and Nusholtz (1984) tests were published the same year and were performed with the same padding in the same test laboratory, partially with the same equipment. However, the mean tendencies are different, with the simulation forces being much more overestimated for Alem. The force is overestimated for all setups with padding although not substantially for some setups (e.g. McIntosh et al., 1993).

Then the fracture status in the test was compared to the failure status in the simulation for the 156 cases selected. A fracture in the model was defined as the erosion of at least one element in the outer cortical solid elements. Erosion occurs when the first principal strain (tension) is larger than the limit set in the model. When considering all simulations in their baseline version (with erosion enabled, Figure 18), the fracture definition correctly classifies 129 tests (57 with failure, 72 without) and yields 17 false positives and 10 false negatives. This leads to a sensitivity of 85% and a specificity of 81%. Most injurious tests are from the Allsop setup while the non-injurious tests are more distributed across studies. If considering only the nineteen high speed tests selected from Raymond and Stark, the sensitivity and specificity decrease slightly due to two false positives and two false negatives in the case of Raymond. When using subject specific models, one false positive and one false negative become correctly predicted (due to the change in scalp thickness), and the sensitivity and specificity increase back.

Overall, despite the peak force mismatches and the inability of the model to describe the experimental variance within each study, the failure criterion captures a substantial part of the fracture status observed in the experiments.

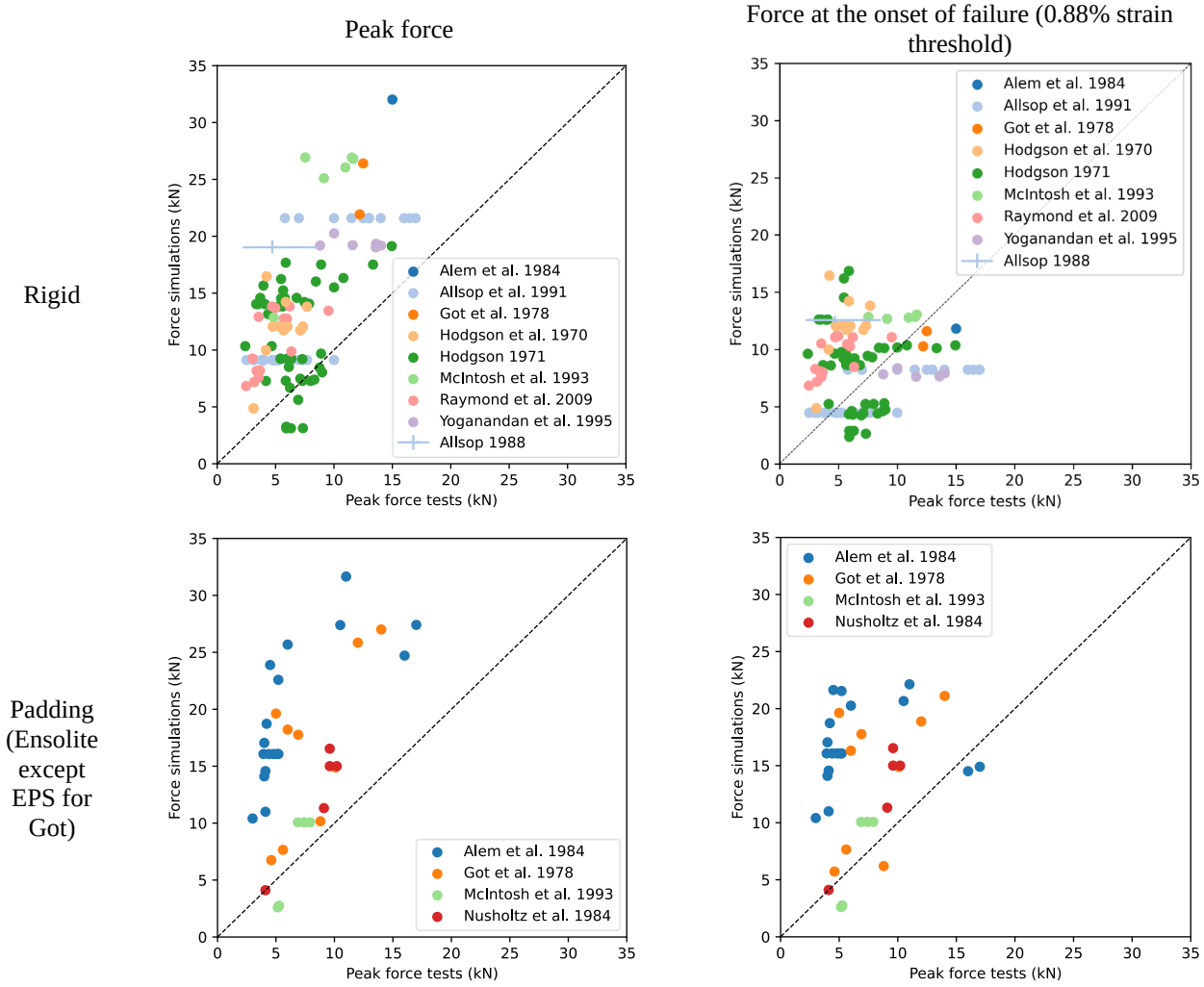

Figure 16. Comparison of peak force (left) and force at the onset of failure (force when the first element is eroded, right) with the peak experimental force. Rigid impactors are at the top and deformable impactors at the bottom.

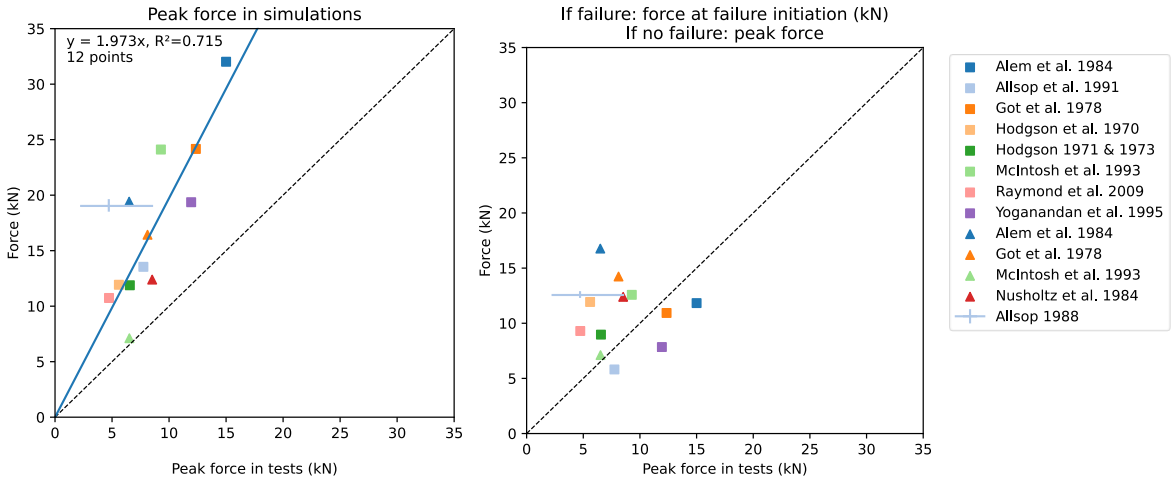

Figure 17. Comparison simulation and experimental forces averaged by study. The peak experimental forces are compared with peak simulation forces (left) or, the forces at the onset of failure when failure occurs (right). The rigid impactors (squares) are separated from the deformable impactors (triangles). Each point is the average of all the points in the corresponding study. Allsop 1988 ranges were not used in the regression. The regression was only plotted to highlight the trend on peak force.

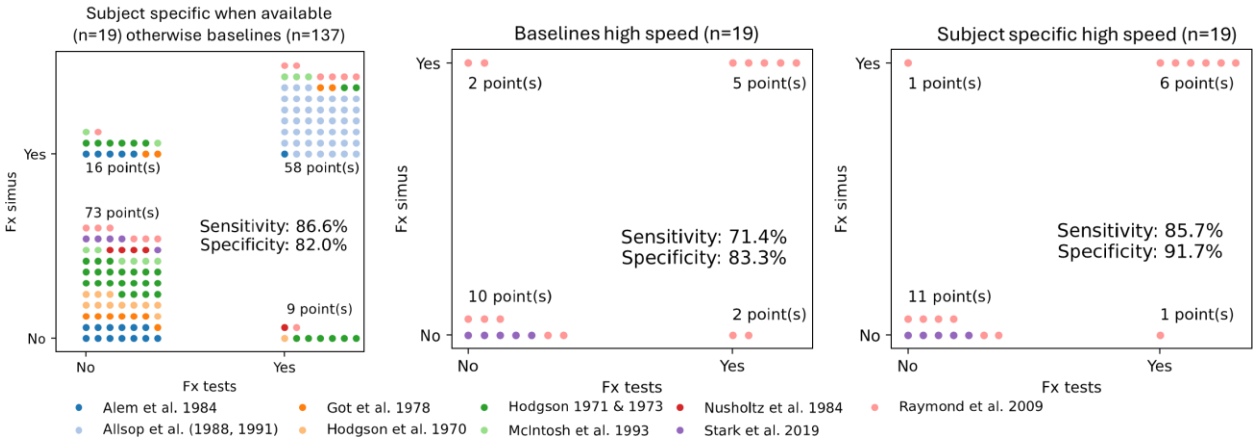

Figure 18. Overview of the skull failure (simulations with erosion enabled, fracture defined as the erosion of at least one solid element of the outer table) vs. PMHS fracture status for the 156 cases selected. As a reminder, Allsop was run at the highest speed of the range provided (4.2 m/s) as all tests were injurious and the exact speed is not provided.

Simulations without failure and strain-based risk curves

The simulations of the 156 load cases selected for injury assessment were repeated with failure/erosion disabled to develop the probabilistic criterion. Peak forces were higher than when failure/erosion was enabled for cases with failed elements, but the difference was only large for cases with the highest force (Figure 19 left). For small peak forces predicted by the model (below 20kN), there were no or small fractures only, and the peak force with or without erosion enabled were close. For higher forces likely associated to more strenuous loading for which larger fractures can be obtained, peak forces with erosion disabled were larger than the ones with erosion disabled. The risk curve based on the simulation peak force with failure disabled is shown in Figure 19 right. A risk of 50% would correspond to a force of 18.9 kN.

Risk curves were then built systematically using all principal strains extracted from all the diploe and all cortical parts of the tables (Figure 20). To facilitate comparisons, the second and third principal strains were made positive in curves and tables. The risk ratios (RR) and associated ratings based on ISO/TS 18506:2014 were close for many curves (values at 10%, 25% and 50% are also provided in Figure 20). The RR were better for strains than for the force, and marginally better for subject specific models than baselines. The lowest RR was obtained for the outer solid second principal strain (shear strain): 0.33

including subject specific models and 0.34 for baselines at 50% risk (n=156). At 50% risk, it was followed by the outer shell and diploe third principal strains (compression, RR of 0.37 and 0.39) although many curves had similar ratios (11 curves between 0.4 and 0.43). The differences between the second principal strain in the outer solids and other metrics were more marked at smaller risks: at 25%, the RR was 0.38 vs. 0.53 for the next best value and, at 10%, it was 0.55 vs. 0.8 for the next best value. Ranking the curves by RR at 10% risk, the three principal strains had curves ranked towards the lowest RR but for different components: if considering the models including subject specific geometry, the three curves with the lower RR were for the 2nd principal in the outer solid, the 3rd principal in the outer shell and the 1st principal in the inner shell (Figure 20 table). The vector patterns corresponding to these strains and part are illustrated for a rigid impact on the top of the head (Figure 21). This combination would correspond to a bending failure mechanism for the outer shells (compression outside, tension inside), with the second principal strain (related to shear) just below the surface of the outer shell.

A few comparisons were made to check the effect of filtering, padding and subject specific models. They are illustrated on the second principal strain in the outer solid in Figure 22. Filtering the peak for possible strain concentrations on a single or few elements did not improve the prediction (Figure 22 left): for the second principal strain in the outer cortical solid, taking the strain of the top 1 element (maximum), until the top 50 increased the RR, perhaps due to the fact the loading area is sometime very small. Fifty elements correspond to the 99.3 percentile of the elements considered, which is larger than the percentiles sometimes used for filtering (e.g. 95th). Using only the rigid impactors had more effect on the risk curve than using subject specific models (Figure 22 center) and slightly reduced the strain at 50% risk (from 0.26 to 0.23 % strain). No comparison could be made with deformable only curves as there is only one fracture in the dataset for deformable objects. Finally, the effect of subject specific modelling was compared using only cases for which subject specific models are available (Raymond et al., 2009, Stark et al., 2019, Figure 22 right, n=19). The effect on the risk curves was more pronounced especially for the lower risk range.

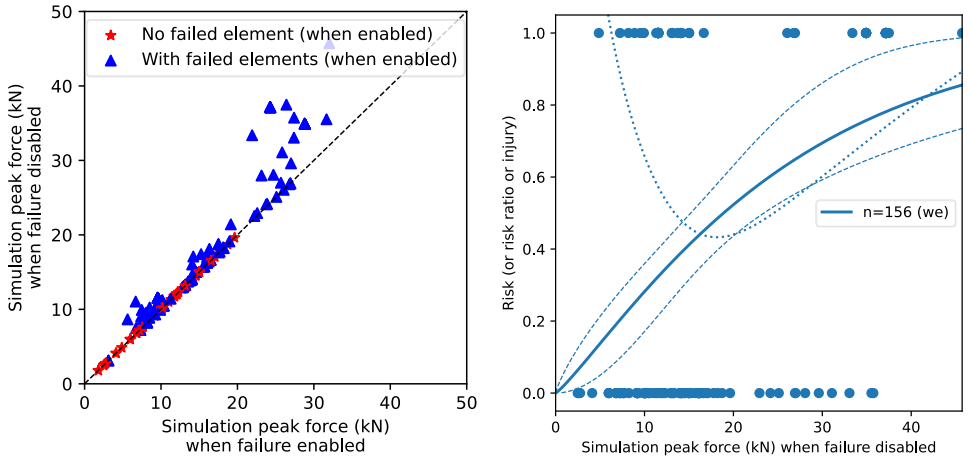

Figure 19. Simulation peak forces with or without failure/erosion enabled (left) and risk curve with confidence intervals (right). The dotted line (right) represents the risk ratio from ISO/TS 18506:2014. The associated ratings are good<0.5<fair<1<marginal<1.5<unacceptable. The best distribution is in parenthesis (we=Weibull). The dots have for abscissa the simulation result and ordinate the test fracture status. Forces at 10%, 25% and 50% risk were 3.7, 8.9 and 18.9 kN, respectively. Corresponding risk ratios were 1.46, 0.74, 0.43.

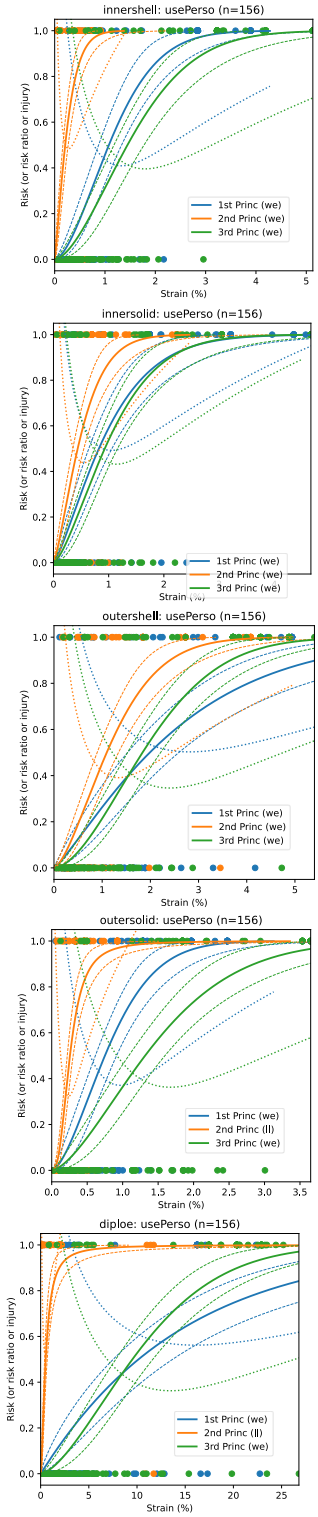

Perso	Strain	Bone	At 10% risk		At 25% risk		At 50% risk	
y/n	Type	part	Strain	Rating	Strain	Rating	Strain	Rating
Perso	2	outer3D	0.11	0.55	0.17	0.38	0.26	0.33
Base	2	outer3D	0.11	0.58	0.16	0.39	0.25	0.34
Perso	3	outer2D	0.62	0.8	1.11	0.53	1.84	0.37
Base	3	outer2D	0.59	0.82	1.08	0.55	1.83	0.38
Perso	1	inner2D	0.35	0.84	0.64	0.57	1.08	0.42
Perso	2	outer2D	0.32	0.85	0.61	0.56	1.09	0.4
Perso	3	inner2D	0.47	0.85	0.85	0.57	1.45	0.41
Base	3	inner2D	0.45	0.87	0.83	0.58	1.43	0.42
Base	1	inner2D	0.32	0.88	0.61	0.59	1.07	0.43
Perso	2	diploe	0.14	0.88	0.27	0.61	0.52	0.53
Base	2	outer2D	0.3	0.89	0.59	0.58	1.08	0.41
Perso	3	diploe	2.88	0.89	5.45	0.59	9.52	0.4
Base	2	diploe	0.14	0.91	0.27	0.63	0.54	0.54
Base	3	diploe	2.83	0.91	5.44	0.6	9.64	0.41
Perso	1	outer3D	0.23	0.92	0.43	0.59	0.75	0.4
Perso	3	outer3D	0.39	0.93	0.75	0.59	1.32	0.39
Base	1	outer3D	0.22	0.95	0.42	0.61	0.74	0.41
Perso	3	inner3D	0.26	0.96	0.51	0.63	0.93	0.45
Base	3	outer3D	0.36	0.97	0.71	0.61	1.3	0.4
Base	3	inner3D	0.24	1	0.51	0.66	0.96	0.46
Perso	1	inner3D	0.19	1.05	0.42	0.7	0.82	0.51
Perso	2	inner3D	0.11	1.05	0.23	0.67	0.44	0.46
Perso	2	inner2D	0.04	1.09	0.1	0.71	0.21	0.51
Base	1	inner3D	0.18	1.13	0.42	0.74	0.87	0.53
Base	2	inner3D	0.1	1.13	0.22	0.72	0.46	0.49
Base	2	inner2D	0.04	1.17	0.1	0.76	0.22	0.53
Perso	1	outer2D	0.41	1.17	0.95	0.77	1.99	0.54
Base	1	outer2D	0.38	1.2	0.92	0.78	1.97	0.54
Perso	1	diploe	1.57	1.35	4.25	0.88	10.16	0.61
Base	1	diploe	1.54	1.39	4.27	0.9	10.43	0.61

Figure 20. Risk curves based on the peak Green St Venant principal strains by part. All curves are based on 156 cases using either the baseline model (base) or subject specific models when available (n=19, perso). The peak second and third principal strains were made positive for the plots. The dotted lines represent the risk ratio from ISO/TS 18506:2014 and the corresponding rating is good<0.5<fair<1<marginal<1.5<unacceptable. The best distribution is in parenthesis (ll=loglog, we=Weibull). As many curves are close from one another, the table on the right provides the strains (in %) and risk ratios at three risk levels.

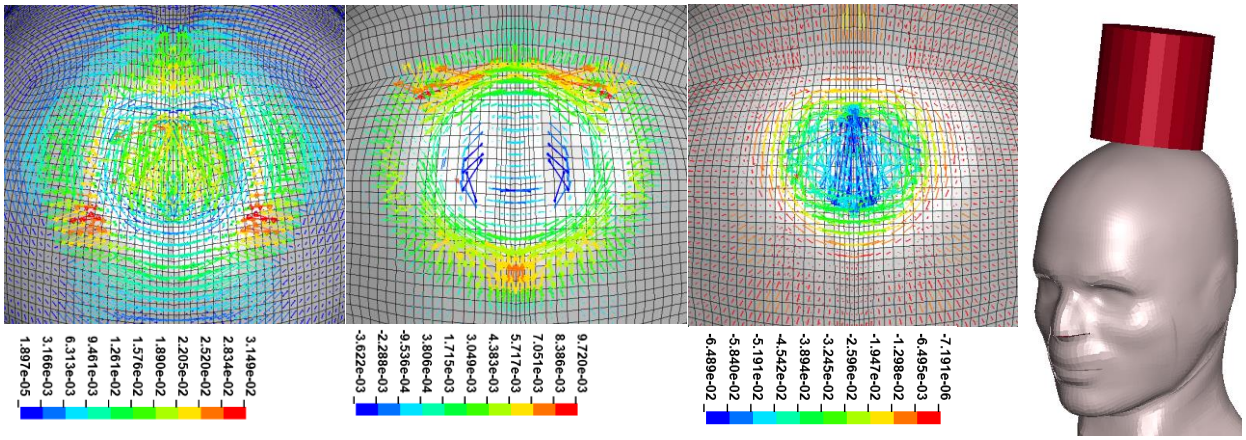

First principal vectors (inner table shells) | Second principal vectors (outer table solid) | Third principal vectors (outer table shells)

Figure 21. Illustration of principal strain vectors following a rigid impact (Alem H409 top, 1.65ms). The first principal (related to tension) is illustrated on the shells of the internal table, the second (related to shear) on the solid of the external table, and the third (related to compression) on the shells of the external table. These combinations of strains and components correspond to the three risk curves with the lower RR at low risk (with subject specific models when available).

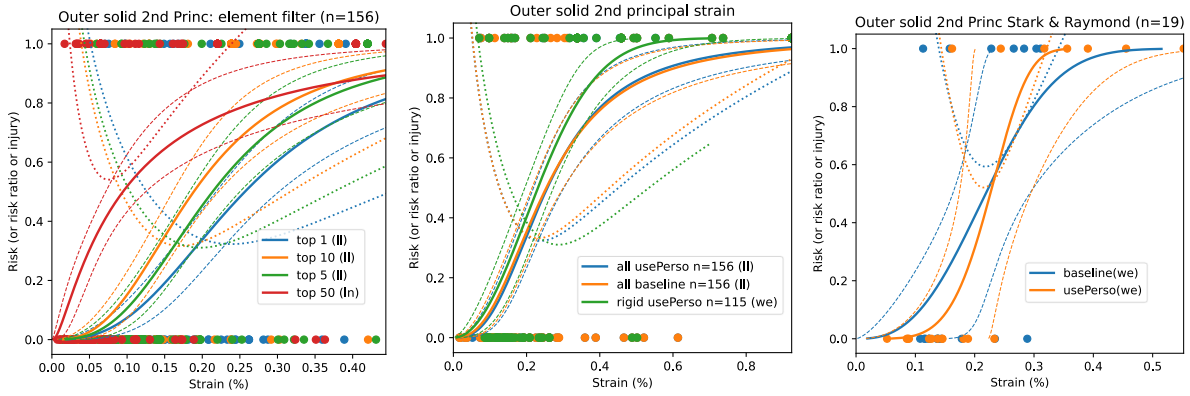

Figure 22. Effects of parameters on the risk curves. The effects are illustrated on the outer solid second principal strain-based risk curves (curves with the best rating). Left: effect of the element filtering (top 1, 5, 10 or 50 element values). Center: effect of subject specific modelling (usePerso) and impactor stiffness. Right: effect of subject specific modelling on the Stark and Raymond datasets. The dotted lines represent the risk ratio from ISO/TS 18506:2014 and the corresponding rating is good<0.5<fair<1<marginal<1.5<unacceptable. The best distribution is in parenthesis (ll=loglog, ln=lognormal, we=Weibull).

DISCUSSION

Over 350 head impact simulations were run with the GHBMC v6.0 head model to assess its response and skull fracture prediction capability. Fracture prediction was based on 156 cases. Both explicit failure representation (with erosion enabled) and probabilistic criterion (with erosion disabled) were tested.

Response / Biofidelity

The peak forces predicted in the simulations were almost always larger than the experimental results, in average by a factor close to 2 based on 12 literature datasets (Figure 17). The difference was especially marked for the rigid impactors, and it was reduced if considering the force at the onset of failure. Differences between some studies could not be explained by the simulations, perhaps due to limitations of the simulation conditions. Variations between PMHS within the same study were not described in most cases. PMHS to PMHS geometrical differences were modelled in the case of Raymond et al. (2009) and Stark et al. (2019) but they did not have a statistically significant effect on the peak force. The effect of the impact location was more marked for both Stark et al. (drone position adjustment) and Raymond et al. (10mm arbitrary shift). It could be hypothesized that such variations could be partially responsible for the experimental variance not captured by the simulation besides biological material properties.

Future improvements may be possible if collecting more documentation about historical studies. This was done in the case of Got et al. (1978) by adjusting the impact location of the padded tests based on camera footage. In the meantime, it seems desirable to consider results in their globality (averaging) and not to consider only a specific study.

Some modelling parameters were investigated for bone and scalp to see if they could explain some of the force discrepancies. Using subject specific models only had a limited effect on the predictions in paired simulations (Figure 21, right), suggesting that skull geometry may not be the primary factor. Skull and scalp material properties could have a more important effect on the responses. Attempts could be made to describe the bone properties using bone density estimates derived from the CT-scans.

First, as the forces were also higher than in Mao et al. (2013) and Lyu et al. (2022), the strain threshold on the cortical bone was lowered from 0.88% to 0.42% (as in older versions of the model). The force magnitude was reduced but it was still higher than both tests and previous simulations. Fully integrated solid elements were also compared to the single integration point solids covered by shells. The peak force was reduced by 20 to 30% in the highest speed case of Raymond et al. (2009). The limited sensitivity to bending of single under-integrated elements may explain some of these differences (behavior after the shell failure). This, and the previous observation of the difference between peak force and the force at the onset of failure raises the issue of de adequacy of failure description by erosion.

Then, various scalp material properties were tested in Raymond's setup. The change of properties between versions of the model or with other models led to peak force variations of a factor between 2 and 3 between extreme cases (Figure 10), with the forces becoming close to the experimental response in the case of the softest response (scalp model of GHBMC v4.1). The changes also affected the extent of element failure. The setup could be especially sensitive to scalp properties as suggested by Raymond et al. (2009) in their analysis.

Vibrations can be visible in the head CG acceleration curves (both numerically and physically) in Stark et al. (2019) tests and corresponding simulations. A modal analysis of the GHBMC skull could be performed to compare the model modes and the natural frequencies of the skull (e.g. as measured in Thomas and Hodgson, 1969).

As the model could not explain some of the differences between studies, change for both bone and scalp should be investigated against the whole simulation database and not only a specific study. The sensitivity analyses allowed to explore the effect of parameters. The use of fully integrated elements for the solids seemed to help and will likely be used in future attempts to improve the biofidelity although it was observed in Raymond et al. (2009) tests that it is likely not the only issue. Other changes regarding bones could include alternative formulations for failure description (e.g. Cronin et al., 2022, Ngan et al., 2024). For the scalp, changes may include softer properties, different boundary conditions (to account for the pericranium and possible scalp sliding) and subject specific scalp geometry from the CT-scans when possible (as it was observed to have an effect in Raymond et al. setup). But without more detailed analysis, it is not possible to point yet which parameters or combination of thereof should be considered as the reason for the overprediction of the force in the current study.

Fracture prediction

Fracture prediction using element failure or a probabilistic approach without element failure were investigated using 156 simulation each. It seemed important to include many tests considering that variations between studies could not always be explained.

Despite the limitations outlined in terms of biofidelity, the model could predict a sizeable proportion of the injuries with both approaches. Results will be discussed using the dataset with subject specific models when available as it is the best representation of what is known of the tests. Eighteen of these nineteen subject specific cases correspond to high-speed tests (ranges: 18.7 – 21.9 m/s for Stark drones, 16.3 – 35.2 m/s for Raymond), the last one being a woodblock test at 5.7m/s.

Using explicit element failure, a sensitivity of 86.6% and a specificity of 82.0% were achieved. There were only 16 false positive and 9 false negative for the 156 cases. Using a probabilistic approach, the second principal strain in the solid of the outer table provided the best risk ratio and rating, especially for low risk levels (0.55 at 10%, 0.38 at 25%). Hence, while the first principal strain is the failure criterion defined for the cortical bone in the model, is not the best predictor and different or combined criteria could be tested for explicit failure description (also related to the discussion on future work related to fracture representation).

Many risk curves were generated and ranked by quality of the fit. By doing this, the strains were considered separately and independently as numerical predictors usable on their own. However, different curves (e.g. tension in the inner table vs. compression in the outer table) may represent better specific loading and injury mechanisms and may be preferable to use in specific scenarios. In that case, combinations may also be useful to improve the prediction of the risk. This should be further investigated.

Most strain-based criteria had better risk ratios than force (all of them for the 10% level, Figure 19 and Figure 20).

Compared to recent efforts in relation to probabilistic criteria, Sahoo et al. (2016) used 86 pedestrian impact cases on a windshield and De Kegel et al. (2019) used 18 rigid pendulum cases (below 6m/s). This study expands on the number of cases (156), speed range (up to 35m/s), and includes rigid, padded and drone impacts. Regarding the prediction accuracy, the current work uses a standardized procedure providing confidence intervals and a quality index which should facilitate future comparisons. The large number of cases included likely helped refine the statistical model and predictions were rated good or fair at low risk level in the sense of the procedure. Compared to previous work, it is hoped that this will facilitate comparisons with future work.

However, the adequacy of the new predictors for drone impact is difficult to assess with certainty. Most simulation cases (138) correspond to low-speed tests (besides the eighteen already mentioned), and most (115) used rigid impactors (while drones are deformable). For the 41 deformable cases, there is always an uncertainty about the modelling of the impactor that we attempted to address through separate test and modelling efforts (Appendices B and C). However, the Ensolite and EPS deformability is different from a drone, and, most importantly, there is only one fracture case for these tests (a test with Ensolite in Nusholtz et al., 1984). This prevents the development or direct assessment of an injury predictor for deformable impactors at high speed. Other padding types could be integrated if they can be modelled (e.g. development of rubber models for Hodgson et al., 1973) but high-speed tests with deformable impactors would be desirable. A test series impactors covered with aluminum honeycomb is under preparation (Pozzi et al., 2024).

In the meantime, the results of rigid and high-speed cases can be separated from all cases to visualize the differences between them (Figure 23). No major discrepancies can be observed at this point. All three have similar sensitivities (around 86%) and specificities between 81 and 92%. The risk curves for all cases and rigid only are similar and intersect the mostly high-speed cases (18/19 of the subject specific models) around 40% risk for the second principal in the outer solid and first principal in inner shell. The intersection is slightly higher (close to 60%) for the third principal in the outer shell. The cases with subject specific models differ more from the other all and rigid only curves for low risks. This does not imply that the difference is due to the speed as the origin of the points, size of datasets, etc. are vastly different.

Strain values at 50% risk for the cortical tables range from 0.7 to 2.0% (first and third principal strain), which is above the average failure strain reported in Wood (1971) of 0.63% in tension. A higher failure strain in compression could be expected in compression based on tension compression testing (e.g. Reilly and Burstein (1975) on the femur). Diploe failure strains, which were associated with worst prediction quality, are much higher but the failure level is more difficult to interpret on cancellous bone depending if the first peak of the response or a point after that peak after some bone compaction has occurred. It is important to remember that the levels predicted by the model are affected by its biofidelity and that no exact match is expected. It can be noted that the levels of the first and third principal strains at 50% risk were typically lower for the cortical solid than the shell covering it (e.g. 0.82% vs 1.08% for the first strains in the inner table, 0.75% vs. 1.84% for the corresponding numbers on the outer table). This could be partially related to a bending mechanism as the strain is measured at the location of the integration point and that, at any given time, the tensile and compressive strains are higher on the outside of the structure. Finally, the 0.88% tensile strain value used as the threshold for erosion in the GHBMC model corresponds to a risk above 50% for the 3D outer cortical table and below 25% for the 2D outer cortical table. Also, as previously shown (Figure 20), the first principal strain used in the definition of the erosion is not the best predictor for the outer table risk curves based on the quality index (but is for the inner table), which also raises questions about the mechanisms described by the model vs. the erosion approach selected.

In the end, the risk curves that were developed are to our knowledge the first simulation based probabilistic risk curve aiming to predict AIS2+ skull fracture on the GHBMC. They use a variety of data and may be useful for future simulations. Assumptions made during the curve development should be checked by

potential users as well as their performance in other loading scenarios. While many risk curves proposed have a good Risk Ratio / quality index in the ISO/TS 18506:2014 sense (at 50% risk and sometimes less), the predictors only target cranial vault fractures due to blunt impact (AIS2+) and no other type of injury were considered. Many curves lead to similar quality index, and it is not known how much difference it would make to use one or another in practical applications. It must be remembered too that the curves are simulation based, i.e. specific to the model version used and likely integrate the limitations in terms of the model biofidelity. Risk curves should therefore not be used with other models or versions (as the strain predictions would differ) and are likely to evolve with improvements of the biofidelity. Using the probabilistic criterion requires disabling element erosion, which also leads to overestimate even more the force in case of severe impact (Figure 19). The effect would not be present for low severity and low risk of fracture. Also, although the development used a variety of impact conditions, the cases available for each potential scenario (e.g. at high speed) limited the development of scenario specific predictors or the rigorous comparison between conditions. Future testing at high speed should help refine these comparisons.

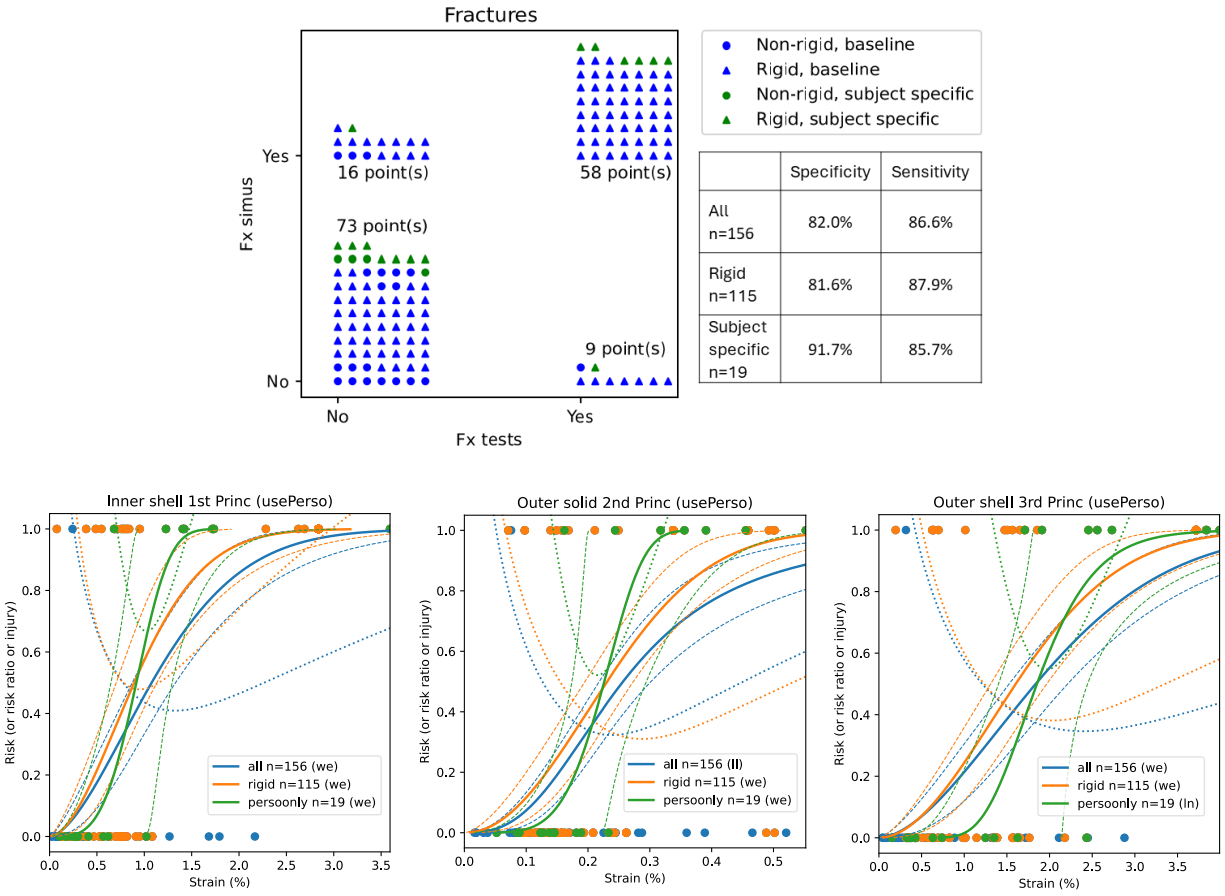

Figure 23. Sensitivity and specificity for simulations with failure enabled (top) and examples of risk curves using three principal strains for the simulation with failure disabled (right). All use the set of simulations with subject specific models when available.

Head mass

Given the inertia of the head, small mass changes could have an effect on the kinematics and the results. The GHBMC head weights 4.67kg, while PMHS head mass in Raymond et al. (2009), Stark et al. (2019) and, Hodgson et al. (1970) and Hodgson & Thomas (1971) studies are 3.40±0.43kg, 3.98±0.15kg, 3.87±0.66kg and 4.72±0.78kg (average ± SD) respectively. Several factors could have contributed to that. First, the exact mass depends on the limit used at the neck by each author and for the model. Then, in some studies, a loss of fluids could be responsible for a weight loss either because the head is segmented in the tests (Raymond et al., 2009) or because fluids are replaced by air (documented by Stark et al., 2009). The density of the head materials could be modified to obtain a correct head mass in the simulations, or the brain mass could be reduced in the model to represent the fluid loss (as performed in Stark et al., 2019).

Limitations

The main limitation concerns the limited knowledge about the boundary conditions. As seen in the movies of the tests in Stark et al. (2019) and Got et al. (1977), there is, in most of the tests, a difference between the desired impact point and the real one, which can lead to large differences in terms of peak force. Moreover, speed censorship has been used in simulations of Allsop et al. (1988) tests: only the largest velocity has been used since only a velocity range is provided in the article. Limitations that could be more easily addressed through setup improvements include a refinement of the neck boundary conditions to better represent the support of the trunk, and the use of subject specific neck curvature in the tests of Stark et al. (2019).

The padding selected for this study (expanded polystyrene and Ensolite) did not lead to injuries, hence limiting their usefulness for the injury analysis. Rubber, used in some of Hodgson et al. (1971, 1977) tests, could also be used but will require developing the model first. Injuries were observed in these tests although after repeating testing.

Regarding the instrumentation and signal analysis, the comparison of the acceleration with Stark et al. is limited by the difference of calculation methodology: direct constrained interpolation for the model, 6aω mount for the PMHS. Hence, the filtering used for the experimental data and the sensors capabilities (e.g. for angular velocities) are not reproduced in the simulation. The comparison could be improved by representing explicitly the mount with each sensor in the model.

Finally, the quantitative comparisons were mostly based on peak force data and no CORA scores were computed. While their calculation could be difficult in many cases in the absence of data for some of the PMHS or the availability of digitized curves without unloading only, their calculation could be helpful in representative cases in the future to help drive and document biofidelity improvements.

CONCLUSIONS

The response and skull fracture prediction capability of an existing finite element of head (GHBMC v6.0) was assessed through a simulation campaign of tests from the literature. The model response was compared to both literature data and previous simulation studies. The fracture prediction capability was assessed using 156 load cases including rigid and deformable impactors, 18 high speed tests and 19 tests for which subject specific models were built.

The model tends to overpredict peak forces, especially for rigid impactors and fracture cases. The formulation of the elements used to describe the skull bone, the bone failure representation (using erosion) and the material properties of the scalp (tissue model) could be further investigated as they affect the response and could help improving the model biofidelity.

Despite these limitations, the model was able to predict a sizable proportion of skull fractures. When simulating failure explicitly, it reached a sensitivity of 86.2% and a specificity of 82% for the 156 cases. When using a probabilistic approach, risk curves could be developed using the principal strains within the bone. The best ratings according to ISO/TS 18506:2014 were obtained for the second principal strain in the solids of the outer table (good at 25 and 50% risk, fair at 10%). The applicability of the risk curve to drone impact conditions (low mass, high speed deformable impactors) is difficult to assess with certainty due to the small number of cases matching these conditions.

Further developments could include refining the boundary conditions of past studies if additional documentation can be obtained, adding literature cases with deformable impactors and injury and conducting high-speed tests with deformable impactors.

ACKNOWLEDGMENTS

This work was supported by the Direction Générale de l'Aviation Civile (DGAC) though the Ground Impact Study II collaborative project with ONERA (Office National d'Études et de Recherches Aérospatiales) and Université Gustave Eiffel. We would like to thank

ONERA for conducting the experimental tests used for the simplified drone model development. We would also like to thank John Bolte from the Ohio State University (OSU) for providing all the data collected during their study on drone impacts (Stark et al., 2019), as well as Dave Raymond (Cal State) and Cynthia Bir (Wayne State University) for providing the CT-scan data of Raymond et al. (2009) study. We would also like to thank the CEESAR for providing data for Got et al. 1978 padded tests, and the National Institute for Aviation Research (NIAR) for supplying data of dummy tests performed during the ASSURE program.

The findings and conclusions of this study are those of the authors and do not necessarily represent the views of the funding organization.

REFERENCES

Alem, N. M., Nusholtz, G. S., & Melvin, J. W. (1984). Head and Neck Response to Axial Impacts. *28th Stapp Car Crash Conference*, 841667. https://doi.org/10.4271/841667

Allsop, D. L., Perl, T. R., & Warner, C. Y. (1991). Force/Deflection and Fracture Characteristics of the Temporo-parietal Region of the Human Head. *35th Stapp Car Crash Conference*, 912907. https://doi.org/10.4271/912907

Allsop, D. L., Warner, C. Y., Wille, M. G., Schneider, D. C., & Nahum, A. M. (1988). Facial Impact Response—A Comparison of the Hybrid III Dummy and Human Cadaver. *SAE Transactions*, 97, 1224–1240.

Arterburn, D. R., Gerardo Olivares, John Bolte, Raj Prabhu, & Stefan Duma. (2019). Task A14: UAS Ground Collision Severity Evaluation 2017-2019. Federal Aviation Administration.

Beillas, P., Giordano, C., Alvarez, V., Li, X., Ying, X., Chevalier, M.-C., Kirscht, S., & Kleiven, S. (2016). Development and performance of the PIPER scalable child human body models.

Berthe, J., Coussa, F., Beillas, P., & Bermond, F. (2019). Drone impact on human beings: Experimental investigation with sUAS. *Conference ASIDIC - Aerospace Structural Impact Dynamics International*, 45 p. https://hal.science/hal-02344606

Chung, L. K., Cheung, Y., Lagman, C., Au Yong, N., McBride, D. Q., & Yang, I. (2017). Skull fracture with effacement of the superior sagittal sinus following drone impact: A case report. *Child's Nervous System*, 33(9), Article 9. https://doi.org/10.1007/s00381-017-3485-z

Cronin, D. S., Watson, B., Khor, F., Gierczycka, D., & Malcolm, S. (2022). Cortical bone continuum damage mechanics constitutive model with stress triaxiality criterion to predict fracture initiation and pattern. *Frontiers in Bioengineering and Biotechnology*, 10, 1022506. https://doi.org/10.3389/fbioe.2022.1022506

De Kegel, D., Meynen, A., Famaey, N., Harry Van Lenthe, G., Depreitere, B., & Sloten, J. V. (2019). Skull fracture prediction through subject-specific finite element modelling is highly sensitive to model parameters. *Journal of the Mechanical Behavior of Biomedical Materials*, 100, 103384. https://doi.org/10.1016/j.jmbbm.2019.103384

European Union Aviation Safety Agency. (2019). Easy Access Rules for Unmanned Aircraft Systems. EU Regulations 2019/947 and 2019/945. Available online. https://www.easa.europa.eu/en/document-library/easy-access-rules/easy-access-rules-unmanned-aircraft-systems-regulations-eu

Federal Aviation Administration. (2020). Executive Summary Final Rule on Operation of Small Unmanned Aircraft Systems Over People. US Federal Register 14 CFR Parts 11, 21, 43, and 107. Available online. https://www.federalregister.gov/documents/2021/01/15/2020-28947/operation-of-small-unmanned-aircraft-systems-over-people

Fedorov, A., Beichel, R., Kalpathy-Cramer, J., Finet, J., Fillion-Robin, J.-C., Pujol, S., Bauer, C., Jennings, D., Fennessy, F., Sonka, M., Buatti, J., Aylward, S., Miller, J. V., Pieper, S., & Kikinis, R. (2012). 3D Slicer as an image computing platform for the Quantitative Imaging Network. *Magnetic Resonance Imaging*, 30(9), 1323–1341. https://doi.org/10.1016/j.mri.2012.05.001

Gayzik F.S., Moreno D.P., Geer C.P., Wuertzer S.D., Martin R.S. and Stitzel J.D. (2011) Development of a full body CAD dataset for computational modeling: a multi-modality approach. *Annals of Biomedical Engineering39*(10):2568-83

Gilles, B., Revéret, L., & Pai, D. K. (2010). Creating and Animating Subject-Specific Anatomical Models. *Computer Graphics Forum*, 29(8), 2340–2351. https://doi.org/10.1111/j.1467-8659.2010.01718.x

Got, C., Patel, A., Fayon, A., Tarrière, C., & Walfisch, G. (1978). Results of Experimental Head Impacts on Cadavers: The Various Data Obtained and Their Relations to Some Measured Physical Parameters. *22nd Stapp Car Crash Conference*, 780887. https://doi.org/10.4271/780887

Hodgson, V. R. (1973). Breaking Strength of The Human Skull Versus Impact Surface Curvature. DOT HS-801 002.

Hodgson, V. R., Brinn, J., Thomas, L. M., & Greenberg, S. W. (1970). Fracture Behavior of the Skull Frontal Bone Against Cylindrical Surfaces. *14th Stapp Car Crash Conference*, 700909. https://doi.org/10.4271/700909

Hodgson, V. R., & Thomas, L. M. (1969). Mechanism of head and neck injury: Final report (Contact No. DA 49-193-MD-2603).

Hodgson, V. R., & Thomas, L. M. (1971). Breaking Strength of the Skull vs. Impact Surface Curvature. 1971. DOT HS-800 583. Contract No. FH-11-7609, Final Report.

John, J., Klug, C., Kranjec, M., Svenning, E., & Iraeus, J. (2022). Hello, world! VIVA+: A human body model lineup to evaluate sex-differences in crash protection. *Frontiers in Bioengineering and Biotechnology*, 10, 918904. https://doi.org/10.3389/fbioe.2022.918904

Khan, A., & Brown, L. (2021). Recreational Drone-Related Injuries in Children: A Review of National Electronic Injury Surveillance System (NEISS) Data. Cureus. https://doi.org/10.7759/cureus.15390

Lindgren, N., Henningsen, M. J., Jacobsen, C., Villa, C., Kleiven, S., & Li, X. (2024). Prediction of skull fractures in blunt force head traumas using finite element head models. *Biomechanics and Modeling in Mechanobiology*, 23(1), 207–225. https://doi.org/10.1007/s10237-023-01768-5

Lyu, D., Zhou, R., Lin, C., Prasad, P., & Zhang, L. (2022). Development and Validation of a New Anisotropic Visco-Hyperelastic Human Head Finite Element Model Capable of Predicting Multiple Brain Injuries. *Frontiers in Bioengineering and Biotechnology*, 10, 831595. https://doi.org/10.3389/fbioe.2022.831595

Mao, H., Zhang, L., Jiang, B., Genthikatti, V. V., Jin, X., Zhu, F., Makwana, R., Gill, A., Jandir, G., Singh, A., & Yang, K. H. (2013). Development of a finite element human head model partially validated with thirty-five experimental cases. *Journal of Biomechanical Engineering*, 135(11), 111002. https://doi.org/10.1115/1.4025101

McIntosh, A. S., Kallieris, D., Mattern, R., & Miltner, E. (1993). Head and Neck Injury Resulting from Low Velocity Direct Impact. *37th Stapp Car Crash Conference* (1993), 933112. https://doi.org/10.4271/933112

Ngan, S., Rampersadh, C., Rycman, A., & Cronin, D. S. (2024). Smoothed particle hydrodynamics implementation to enhance vertebral fracture finite element model in a cervical spine segment under compression. *Journal of the Mechanical Behavior of Biomedical Materials*, 151, 106412. https://doi.org/10.1016/j.jmbbm.2024.106412

Nusholtz, G. S., Lux, P., Kaiker, P., & Janicki, M. A. (1984). Head impact Response—Skull Deformation and Angular Accelerations. *28th Stapp Car Crash Conference*, 841657. https://doi.org/10.4271/841657

Petitjean, A., Trosseille, X., Praxl, N., Hynd, D., & Irwin, A. (2012). Injury risk curves for the WorldSID 50th male dummy. *Stapp Car Crash Journal*, 56, 323–347. https://doi.org/10.4271/2009-22-0016

Pozzi, C., Paccard, B., Bermond, F., & Beillas, P. (2022). Fracture sensitivity of a human head model in surrogate drone impacts. *IRCOBI 2022 Conference, International Research Council on Biomechanics of Injury*, 2022, 2p. https://hal.science/hal-03788831

Pozzi, C., Ragonet, M., Bermond, F., Coussa, F., & Beillas, P. (2024). Adjusting Drone Surrogate properties for PMHS testing: Experimental response and numerical model. *IRCOBI 2024 Conference, International Research Council on Biomechanics of Injury*, 2024.

Prasad, P., & Mertz, H. J. (1985). The Position of the United States Delegation to the ISO Working Group 6 on the Use of HIC in the Automotive Environment. *SAE transactions*, 106-116. 851246. https://doi.org/10.4271/851246

R Core Team. (2018). R: A language and environment for statistical computing. R Foundation for Statistical Computing, Vienna, Austria. https://www.R-project.org/

Rattanagraikanakorn, B., Blom, H. A., Sharpanskykh, A., De Wagter, C., Jiang, C., Schuurman, M. J.,

Gransden, D. I., & Happee, R. (2020a, June 15). Modeling and Simulating Human Fatality due to Quadrotor UAS Impact. *AIAA Aviation 2020 forum*. https://doi.org/10.2514/6.2020-2902

Rattanagraikanakorn, B., Gransden, D. I., Schuurman, M., De Wagter, C., Happee, R., Sharpanskykh, A., & Blom, H. A. P. (2020b, November 1). Multibody system modelling of unmanned aircraft system collisions with the human head. *International Journal of Crashworthiness*, 689–707.

Rattanagraikanakorn, B., Schuurman, M., Gransden, D. I., Happee, R., De Wagter, C., Sharpanskykh, A., & Blom, H. A. P. (2022). Modelling head injury due to unmanned aircraft systems collision: Crash dummy vs human body. *International Journal of Crashworthiness*, 27(2), 400–413. https://doi.org/10.1080/13588265.2020.1807687

Rattanagraikanakorn, B., Schuurman, M. J., Gransden, D. I., Happee, R., De Wagter, C., Sharpanskykh, A., & Blom, H. A. (2019, June 17). Modelling Head Injury due to Unmanned Aircraft Systems Collision: Crash Dummy vs Human Body. *AIAA Aviation 2019 Forum, Dallas, Texas*. https://doi.org/10.2514/6.2019-2835

Raymond, D., Van Ee, C., Crawford, G., & Bir, C. (2009). Tolerance of the skull to blunt ballistic temporo-parietal impact. *Journal of Biomechanics*, 42(15), 2479–2485. https://doi.org/10.1016/j.jbiomech.2009.07.018

Reilly, D. T., & Burstein, A. H. (1975). The elastic and ultimate properties of compact bone tissue. *Journal of Biomechanics*, 8(6), 393–405. https://doi.org/10.1016/0021-9290(75)90075-5

Sahoo, D., Deck, C., Yoganandan, N., & Willinger, R. (2016). Development of skull fracture criterion based on real-world head trauma simulations using finite element head model. *Journal of the Mechanical Behavior of Biomedical Materials*, 57, 24–41. https://doi.org/10.1016/j.jmbbm.2015.11.014

SESAR Joint Undertaking. (2017). European drones outlook study: Unlocking the value for Europe. Publications Office. https://data.europa.eu/doi/10.2829/085259

Stark, D. B., Willis, A. K., Eshelman, Z., Kang, Y.-S., Ramachandra, R., Bolte, J. H., & McCrink, M. (2019). Human Response and Injury Resulting from Head Impacts with Unmanned Aircraft Systems. *Stapp Car Crash Journal, 63*, 29–64. https://doi.org/10.4271/2019-22-0002

Wood, J. L. (1971). Dynamic response of human cranial bone. *Journal of Biomechanics*, 4(1), 1–12. https://doi.org/10.1016/0021-9290(71)90010-8

Yoganandan, N., Pintar, F. A., Sances, A., Walsh, P. R., Ewing, C. L., Thomas, D. J., & Snyder, R. G. (1995). Biomechanics of Skull Fracture. *Journal of Neurotrauma*, 12(4), 659–668.

APPENDIX A. DETAILED SIMULATION MATRIX

Table 4. Detailed simulation matrix. In the impactor stiffness column, "Ens". significates Ensolite. In the location column, "Par." significates parietal and "Temp." significates temporal.

Reference	Test	Injury assessment	Force comp.	Impact. stiff.	Vel. (m/s)	Loc.	Angle (deg)	Force (kN)	Fx	Baseline (failure enabled)	Baseline (failure disabled)	Subject specific	Base.	Subject specific	Baseline (skull outer 3D only)	Subject specific (skull outer 3D only)
								Test		Force (simulation)			Fracture (simulation)			
Alem et al. 1984	H201	Yes (1 test/PMHS)	Yes	Ens.	8	Top	0	5.1	0	16.1	16.1		0	0		
Alem et al. 1984	H202	Yes (1 test/PMHS)	Yes	Ens.	8	Top	0	5.2	0	16.1	16.1		0	0		
Alem et al. 1984	H203	Yes (1 test/PMHS)	Yes	Ens.	8	Top	0	4.4	0	16.1	16.1		0	0		
Alem et al. 1984	H204	Yes (1 test/PMHS)	Yes	Ens.	8	Top	0	3.9	0	16.1	16.1		0	0		
Alem et al. 1984	H205	Yes (1 test/PMHS)	Yes	Ens.	8	Top	0	4.8	0	16.1	16.1		0	0		
Alem et al. 1984	H401	Yes (1 test/PMHS)	Yes	Ens.	8.4	Top	0	4.2	0	18.7	18.7		0	0		
Alem et al. 1984	H402	Yes (1 test/PMHS)	Yes	Ens.	10.9	Top	0	11.0	0	31.7	35.5		1	1		
Alem et al. 1984	H403	Yes (1 test/PMHS)	Yes	Ens.	10.9	Front	0	10.5	0	27.4	33.1		1	1		
Alem et al. 1984	H404	Yes (1 test/PMHS)	Yes	Ens.	7.8	Front	0	4.0	0	14.1	14.1		0	0		
Alem et al. 1984	H405	Yes (1 test/PMHS)	Yes	Ens.	7.7	Front	0	4.1	0	14.6	14.6		0	0		
Alem et al. 1984	H406	Yes (1 test/PMHS)	Yes	Ens.	8	Front	0	4.0	0	17.0	17.0		0	0		
Alem et al. 1984	H407	Yes (1 test/PMHS)	Yes	Ens.	9.2	Top	0	4.5	0	23.9	24.2		1	0		
Alem et al. 1984	H408	Yes (1 test/PMHS)	Yes	Ens.	9.7	Front	0	6.0	0	25.7	27.0		1	1		
Alem et al. 1984	H409	Yes (1 test/PMHS)	Yes	Rigid	10.4	Top	0	15.0	1	32.0	45.7		1	1		
Alem et al. 1984	H410	Yes (1 test/PMHS)	Yes	Ens.	9	Top	0	5.2	0	22.6	22.9		1	0		

Reference	Test	Injury assessment	Force comp.	Impact. stiff.	Vel. (m/s)	Loc.	Angle (deg)	Force (kN)	Fx	Baseline (failure enabled)	Baseline (failure disabled)	Subject specific	Base.	Subject specific	Baseline (skull outer 3D only)	Subject specific (skull outer 3D only)
								Test		Force (simulation)			Fracture (simulation)			
Alem et al. 1984	H411	Yes (1 test/PMHS)	Yes	Ens.	7.2	Top	0	4.1	0	11.0	11.0		0	0		
Alem et al. 1984	H412	Yes (1 test/PMHS)	Yes	Ens.	7.1	Top	0	3.0	0	10.4	10.4		0	0		
Alem et al. 1984	H413	Yes (1 test/PMHS)	Yes	Ens.	9	Top	0	17.0	0	27.4	35.7		1	1		
Alem et al. 1984	H414	Yes (1 test/PMHS)	Yes	Ens.	6.9	Top	0	16.0	0	24.7	28.1		1	1		
Allsop et al. 1991	F25746	Yes (1 test/PMHS)	Yes	Rigid	4.3	Par.	0	5.8	1	28.8	34.9		1	1		
Allsop et al. 1991	F26378	Yes (1 test/PMHS)	Yes	Rigid	4.3	Par.	0	7.0	1	28.8	34.9		1	1		
Allsop et al. 1991	M25744	Yes (1 test/PMHS)	Yes	Rigid	4.3	Par.	0	10.0	1	28.8	34.9		1	1		
Allsop et al. 1991	F26107	Yes (1 test/PMHS)	Yes	Rigid	4.3	Par.	0	11.5	1	28.8	34.9		1	1		
Allsop et al. 1991	F26341	Yes (1 test/PMHS)	Yes	Rigid	4.3	Par.	0	12.5	1	28.8	34.9		1	1		
Allsop et al. 1991	M25725	Yes (1 test/PMHS)	Yes	Rigid	4.3	Par.	0	13.0	1	28.8	34.9		1	1		
Allsop et al. 1991	F26379	Yes (1 test/PMHS)	Yes	Rigid	4.3	Par.	0	13.0	1	28.8	34.9		1	1		
Allsop et al. 1991	F26115	Yes (1 test/PMHS)	Yes	Rigid	4.3	Par.	0	14.0	1	28.8	34.9		1	1		
Allsop et al. 1991	M25794	Yes (1 test/PMHS)	Yes	Rigid	4.3	Par.	0	16.0	1	28.8	34.9		1	1		
Allsop et al. 1991	F26352	Yes (1 test/PMHS)	Yes	Rigid	4.3	Par.	0	16.5	1	28.8	34.9		1	1		
Allsop et al. 1991	M26338	Yes (1 test/PMHS)	Yes	Rigid	4.3	Par.	0	17.0	1	28.8	34.9		1	1		
Allsop et al. 1991	F26588	Yes (1 test/PMHS)	Yes	Rigid	2.7	Temp.	0	2.5	1	9.6	11.5		1	1		
Allsop et al. 1991	M26903	Yes (1 test/PMHS)	Yes	Rigid	2.7	Temp.	0	3.1	1	9.6	11.5		1	1		

Reference	Test	Injury assessment	Force comp.	Impact. stiff.	Vel. (m/s)	Loc.	Angle (deg)	Force (kN)	Fx	Baseline (failure enabled)	Baseline (failure disabled)	Subject specific	Base.	Subject specific	Baseline (skull outer 3D only)	Subject specific (skull outer 3D only)
								Test		Force (simulation)			Fracture (simulation)			
Allsop et al. 1991	F26342	Yes (1 test/PMHS)	Yes	Rigid	2.7	Temp.	0	3.2	1	9.6	11.5		1	1		
Allsop et al. 1991	F26374	Yes (1 test/PMHS)	Yes	Rigid	2.7	Temp.	0	3.8	1	9.6	11.5		1	1		
Allsop et al. 1991	F26380	Yes (1 test/PMHS)	Yes	Rigid	2.7	Temp.	0	4.0	1	9.6	11.5		1	1		
Allsop et al. 1991	M26922	Yes (1 test/PMHS)	Yes	Rigid	2.7	Temp.	0	4.0	1	9.6	11.5		1	1		
Allsop et al. 1991	F26377	Yes (1 test/PMHS)	Yes	Rigid	2.7	Temp.	0	4.0	1	9.6	11.5		1	1		
Allsop et al. 1991	F26371	Yes (1 test/PMHS)	Yes	Rigid	2.7	Temp.	0	4.7	1	9.6	11.5		1	1		
Allsop et al. 1991	M26329	Yes (1 test/PMHS)	Yes	Rigid	2.7	Temp.	0	4.8	1	9.6	11.5		1	1		
Allsop et al. 1991	F26361	Yes (1 test/PMHS)	Yes	Rigid	2.7	Temp.	0	4.8	1	9.6	11.5		1	1		
Allsop et al. 1991	M26383	Yes (1 test/PMHS)	Yes	Rigid	2.7	Temp.	0	5.0	1	9.6	11.5		1	1		
Allsop et al. 1991	F26925	Yes (1 test/PMHS)	Yes	Rigid	2.7	Temp.	0	5.1	1	9.6	11.5		1	1		
Allsop et al. 1991	F26587	Yes (1 test/PMHS)	Yes	Rigid	2.7	Temp.	0	5.2	1	9.6	11.5		1	1		
Allsop et al. 1991	F26384	Yes (1 test/PMHS)	Yes	Rigid	2.7	Temp.	0	5.3	1	9.6	11.5		1	1		
Allsop et al. 1991	F26573	Yes (1 test/PMHS)	Yes	Rigid	2.7	Temp.	0	6.0	1	9.6	11.5		1	1		
Allsop et al. 1991	M26350	Yes (1 test/PMHS)	Yes	Rigid	2.7	Temp.	0	6.4	1	9.6	11.5		1	1		
Allsop et al. 1991	F26354	Yes (1 test/PMHS)	Yes	Rigid	2.7	Temp.	0	7.0	1	9.6	11.5		1	1		
Allsop et al. 1991	M26372	Yes (1 test/PMHS)	Yes	Rigid	2.7	Temp.	0	7.3	1	9.6	11.5		1	1		
Allsop et al. 1991	M26368	Yes (1 test/PMHS)	Yes	Rigid	2.7	Temp.	0	7.7	1	9.6	11.5		1	1		

Reference	Test	Injury assessment	Force comp.	Impact. stiff.	Vel. (m/s)	Loc.	Angle (deg)	Force (kN)	Fx	Baseline (failure enabled)	Baseline (failure disabled)	Subject specific	Base.	Subject specific	Baseline (skull outer 3D only)	Subject specific (skull outer 3D only)
								Test		Force (simulation)			Fracture (simulation)			
Allsop et al. 1991	M25373	Yes (1 test/PMHS)	Yes	Rigid	2.7	Temp.	0	10.0	1	9.6	11.5		1	1		
Allsop et al. 1988	2308	Yes (1 test/PMHS)	Yes	Rigid	4.2	Front	0	5.2	1	24.3	37.2		1	1		
Allsop et al. 1988	2215	Yes (1 test/PMHS)	Yes	Rigid	4.2	Front	0	2.6	1	24.3	37.2		1	1		
Allsop et al. 1988	2278	Yes (1 test/PMHS)	Yes	Rigid	4.2	Front	0	2.8	1	24.3	37.2		1	1		
Allsop et al. 1988	2185	Yes (1 test/PMHS)	Yes	Rigid	4.2	Front	0	2.2	1	24.3	37.2		1	1		
Allsop et al. 1988	2225	Yes (1 test/PMHS)	Yes	Rigid	4.2	Front	0	4.0	1	24.3	37.2		1	1		
Allsop et al. 1988	2201	Yes (1 test/PMHS)	Yes	Rigid	4.2	Front	0	4.8	1	24.3	37.2		1	1		
Allsop et al. 1988	2291	Yes (1 test/PMHS)	Yes	Rigid	4.2	Front	0	8.6	1	24.3	37.2		1	1		
Allsop et al. 1988	2289	Yes (1 test/PMHS)	Yes	Rigid	4.2	Front	0	4.3	1	24.3	37.2		1	1		
Allsop et al. 1988	2245	Yes (1 test/PMHS)	Yes	Rigid	4.2	Front	0	4.5	1	24.3	37.2		1	1		
Allsop et al. 1988	2151	Yes (1 test/PMHS)	Yes	Rigid	4.2	Front	0	4.3	1	24.3	37.2		1	1		
Allsop et al. 1988	2297	Yes (1 test/PMHS)	Yes	Rigid	4.2	Front	0	6.5	1	24.3	37.2		1	1		
Allsop et al. 1988	2292	Yes (1 test/PMHS)	Yes	Rigid	4.2	Front	0	6.0	1	24.3	37.2		1	1		
Allsop et al. 1988	2230	Yes (1 test/PMHS)	Yes	Rigid	4.2	Front	0	5.5	1	24.3	37.2		1	1		
Got et al. 1978	68	Yes (1 test/PMHS)	Yes	Rigid	5.99	Par.	0	12.2	1	21.9	33.4		1	1		
Got et al. 1978	76	Yes (1 test/PMHS)	Yes	Rigid	7	Par.	0	12.5	1	26.4	37.5		1	1		
Got et al. 1978	134	Yes (1 test/PMHS)	Yes	EPS (21g/L)	7.67	Front	0	8.8	0	10.2	11.2		1	0		

Reference	Test	Injury assessment	Force comp.	Impact. stiff.	Vel. (m/s)	Loc.	Angle (deg)	Force (kN)	Fx	Baseline (failure enabled)	Baseline (failure disabled)	Subject specific	Base.	Subject specific	Baseline (skull outer 3D only)	Subject specific (skull outer 3D only)
								Test		Force (simulation)			Fracture (simulation)			
Got et al. 1978	140	Yes (1 test/PMHS)	Yes	EPS (21g/L)	7.67	Front	0	6.0	0	18.2	18.2		1	0		
Got et al. 1978	141	Yes (1 test/PMHS)	Yes	EPS (21g/L)	7.67	Front	0	12.0	0	25.8	31.1		1	1		
Got et al. 1978	142	Yes (1 test/PMHS)	Yes	EPS (21g/L)	7.67	Front	0	14.0	0	27.0	29.6		1	1		
Got et al. 1978	143	Yes (1 test/PMHS)	Yes	EPS (21g/L)	7.67	Front	0	5.6	0	7.7	7.7		0	0		
Got et al. 1978	144	Yes (1 test/PMHS)	Yes	EPS (21g/L)	7.67	Front	0	4.6	0	6.8	7.5		1	0		
Got et al. 1978	145	Yes (1 test/PMHS)	Yes	EPS (25g/L)	7.67	Par.	0	10.1	0	14.9	14.9		0	0		
Got et al. 1978	146	Yes (1 test/PMHS)	Yes	EPS (25g/L)	7.67	Par.	0	6.9	0	17.8	17.8		0	0		
Got et al. 1978	147	Yes (1 test/PMHS)	Yes	EPS (25g/L)	7.67	Par.	0	5.0	0	19.6	19.6		0	0		
Hodgson et al. 1970	1486a	Yes (strongest w.o injury)	No data	Rigid	2.74	Front	45		0	12.1	12.1		0	0		
Hodgson et al. 1970	1486b	No (>1 test and injury)	Yes	Rigid	3.14	Front	45	5.9	1	14.2	14.2		0	0		
Hodgson et al. 1970	1504a	Yes (strongest w.o injury)	No data	Rigid	2.23	Front	45		0	9.2	9.2		0	0		
Hodgson et al. 1970	1504b	No (>1 test and injury)	Yes	Rigid	2.74	Front	45	5.9	1	12.1	12.1		0	0		
Hodgson et al. 1970	1536a	Yes (strongest w.o injury)	No data	Rigid	2.23	Front	45		0	9.2	9.2		0	0		
Hodgson et al. 1970	1536b	No (>1 test and injury)	Yes	Rigid	2.74	Front	45	5.3	1	12.1	12.1		0	0		
Hodgson et al. 1970	1581a	Yes (strongest w.o injury)	No data	Rigid	3.14	Front	45		0	14.2	14.2		0	0		
Hodgson et al. 1970	1581b	No (>1 test and injury)	Yes	Rigid	3.54	Front	45	4.2	1	16.5	16.5		0	0		
Hodgson et al. 1970	1582a	Yes (strongest w.o injury)	No data	Rigid	2.23	Front	45		0	9.2	9.2		0	0		

Reference	Test	Injury assessment	Force comp.	Impact. stiff.	Vel. (m/s)	Loc.	Angle (deg)	Force (kN)	Fx	Baseline (failure enabled)	Baseline (failure disabled)	Subject specific	Base.	Subject specific	Baseline (skull outer 3D only)	Subject specific (skull outer 3D only)
								Test		Force (simulation)			Fracture (simulation)			
Hodgson et al. 1970	1582b	No (>1 test and injury)	Yes	Rigid	2.74	Front	45	6.0	1	12.1	12.1		0	0		
Hodgson et al. 1970	1589a	Yes (strongest w.o injury)	No data	Rigid	2.23	Front	45		0	9.2	9.2		0	0		
Hodgson et al. 1970	1589b	No (>1 test and injury)	Yes	Rigid	2.74	Front	45	7.3	1	12.1	12.1		0	0		
Hodgson et al. 1970	1615a	Yes (strongest w.o injury)	No data	Rigid	2.23	Front	45		0	9.2	9.2		0	0		
Hodgson et al. 1970	1615b	No (>1 test and injury)	Yes	Rigid	2.74	Front	45	4.8	1	12.1	12.1		0	0		
Hodgson et al. 1970	1471a	Yes (strongest w.o injury)	No data	Rigid	2.74	Front	45		0	10.0	10.0		0	0		
Hodgson et al. 1970	1471b	No (>1 test and injury)	Yes	Rigid	3.14	Front	45	7.1	1	11.7	11.7		0	0		
Hodgson et al. 1970	1584b	Yes (1 test/PMHS)	Yes	Rigid	1.58	Front	45	3.1	1	4.9	4.9		0	0		
Hodgson et al. 1970	1596a	Yes (strongest w.o injury)	No data	Rigid	3.14	Front	45		0	11.7	11.7		0	0		
Hodgson et al. 1970	1596b	No (>1 test and injury)	Yes	Rigid	3.54	Front	45	7.7	1	13.8	13.8		0	0		
Hodgson et al. 1970	1614a	Yes (strongest w.o injury)	No data	Rigid	2.74	Front	45		0	10.0	10.0		0	0		
Hodgson et al. 1970	1614b	No (>1 test and injury)	Yes	Rigid	3.14	Front	45	5.7	1	11.7	11.7		0	0		
Hodgson et al. 1970	1616a	Yes (strongest w.o injury)	No data	Rigid	2.23	Front	45		0	7.7	7.7		0	0		
Hodgson et al. 1970	1616b	No (>1 test and injury)	Yes	Rigid	2.74	Front	45	4.2	1	10.0	10.0		0	0		
Hodgson 1971 & 1973	1717	Yes (strongest w.o injury)	No data	Rigid	2.23	Front	0		0	9.2	9.2		0	0		
Hodgson 1971 & 1973	1747	Yes (strongest w.o injury)	No data	Rigid	1.58	Front	0		0	6.0	6.0		0	0		
Hodgson 1971 & 1973	1701	Yes (strongest w.o injury)	No data	Rigid	1.58	Front	0		0	6.0	6.0		0	0		

Reference	Test	Injury assessment	Force comp.	Impact. stiff.	Vel. (m/s)	Loc.	Angle (deg)	Force (kN)	Fx	Baseline (failure enabled)	Baseline (failure disabled)	Subject specific	Base.	Subject specific	Baseline (skull outer 3D only)	Subject specific (skull outer 3D only)
								Test		Force (simulation)			Fracture (simulation)			
Hodgson 1971 & 1973	1699	Yes (strongest w.o injury)	No data	Rigid	1.58	Front	0		0	6.0	6.0		0	0		
Hodgson 1971 & 1973	1820	Yes (strongest w.o injury)	No data	Rigid	3.14	Temp.	0		0	14.4	15.3		1	0		
Hodgson 1971 & 1973	1819	Yes (strongest w.o injury)	No data	Rigid	1.58	Temp.	0		0	6.8	6.8		0	0		
Hodgson 1971 & 1973	1821	Yes (strongest w.o injury)	No data	Rigid	1.58	Temp.	0		0	6.8	6.8		0	0		
Hodgson 1971 & 1973	1829	Yes (strongest w.o injury)	No data	Rigid	2.23	Temp.	0		0	10.3	10.5		1	0		
Hodgson 1971 & 1973	44	Yes (strongest w.o injury)	No data	Rigid	2.23	Temp.	0		0	10.3	10.5		1	0		
Hodgson 1971 & 1973	57	Yes (strongest w.o injury)	No data	Rigid	3.51	Temp.	0		0	16.0	17.1		1	0		
Hodgson 1971 & 1973	1848	Yes (strongest w.o injury)	No data	Rigid	2.23	Front	0		0	7.3	7.2		1	0		
Hodgson 1971 & 1973	1838	Yes (1 test/PMHS)	Yes	Rigid	2.23	Front	0	4.2	1	7.3	7.2		1	0		
Hodgson 1971 & 1973	1841	Yes (strongest w.o injury)	No data	Rigid	2.23	Front	0		0	7.3	7.2		1	0		
Hodgson 1971 & 1973	1862	Yes (strongest w.o injury)	No data	Rigid	2.87	Front	0		0	9.2	10.0		1	1		
Hodgson 1971 & 1973	1876	Yes (strongest w.o injury)	No data	Rigid	2.87	Front	0		0	9.2	10.0		1	1		
Hodgson 1971 & 1973	1875	Yes (strongest w.o injury)	No data	Rigid	2.87	Front	0		0	9.2	10.0		1	1		
Hodgson 1971 & 1973	1859	Yes (1 test/PMHS)	Yes	Rigid	2.87	Front	0	3.5	1	14.0	14.0		1	0		
Hodgson 1971 & 1973	1871	Yes (1 test/PMHS)	Yes	Rigid	2.87	Front	0	4.1	1	14.0	14.0		1	0		
Hodgson 1971 & 1973	1861	Yes (strongest w.o injury)	No data	Rigid	2.87	Front	0		0	14.0	14.0		1	0		
Hodgson 1971 & 1973	1843	Yes (strongest w.o injury)	No data	Rigid	3.14	Front	0		0	15.7	15.7		1	0		

Reference	Test	Injury assessment	Force comp.	Impact. stiff.	Vel. (m/s)	Loc.	Angle (deg)	Force (kN)	Fx	Baseline (failure enabled)	Baseline (failure disabled)	Subject specific	Base.	Subject specific	Baseline (skull outer 3D only)	Subject specific (skull outer 3D only)
								Test		Force (simulation)			Fracture (simulation)			
Hodgson 1971 & 1973	1857	Yes (strongest w.o injury)	No data	Rigid	3.14	Front	0		0	14.0	14.2		1	1		
Hodgson 1971 & 1973	1890	Yes (strongest w.o injury)	No data	Rigid	2.87	Front	0		0	13.2	13.3		1	0		
Hodgson 1971 & 1973	1905	Yes (strongest w.o injury)	No data	Rigid	2.87	Front	0		0	13.2	13.3		1	0		
Hodgson 1971 & 1973	1906	Yes (1 test/PMHS)	Yes	Rigid	3.14	Front	0	5.8	1	14.6	15.0		1	0		
Hodgson 1971 & 1973	1910	Yes (strongest w.o injury)	No data	Rigid	3.14	Front	0		0	14.6	15.0		1	0		
Hodgson 1971 & 1973	2068	Yes (strongest w.o injury)	No data	Rigid	2.23	Front	0		0	10.1	10.1		0	0		
Hodgson 1971 & 1973	2067	Yes (strongest w.o injury)	No data	Rigid	2.96	Front	0		0	14.5	14.5		0	0		
Hodgson 1971 & 1973	2108	Yes (strongest w.o injury)	No data	Rigid	3.32	Front	0		0	16.5	16.7		1	0		
Hodgson 1971 & 1973	2182	Yes (1 test/PMHS)	Yes	Rigid	3.05	Front	0	5.9	1	15.0	15.0		0	0		
Hodgson 1971 & 1973	1930	Yes (1 test/PMHS)	Yes	Rigid	3.32	Front	0	5.9	1	16.5	16.7		1	0		
Hodgson 1971 & 1973	2246	Yes (1 test/PMHS)	Yes	Rigid	2.96	Front	0	9.0	1	8.0	9.5		1	1		
Hodgson 1971 & 1973	2268	Yes (1 test/PMHS)	Yes	Rigid	2.83	Front	0	8.8	1	8.5	8.9		1	1		
Hodgson 1971 & 1973	2146	Yes (strongest w.o injury)	No data	Rigid	2.87	Front	0		0	13.9	14.1		1	0		
Hodgson 1971 & 1973	2248	Yes (strongest w.o injury)	No data	Rigid	3.23	Front	0		0	16.0	16.3		1	1		
Hodgson 1971 & 1973	2242	Yes (strongest w.o injury)	No data	Rigid	3.23	Front	0		0	16.0	16.3		1	1		
Hodgson 1971 & 1973	2	No (>1 test and injury)	Yes	Rigid	2.23	Front	0	6.0	1	9.2	9.2		0	0		
Hodgson 1971 & 1973	3	No (>1 test and injury)	Yes	Rigid	2.23	Front	0	5.4	1	9.2	9.2		1	0		

Reference	Test	Injury assessment	Force comp.	Impact. stiff.	Vel. (m/s)	Loc.	Angle (deg)	Force (kN)	Fx	Baseline (failure enabled)	Baseline (failure disabled)	Subject specific	Base.	Subject specific	Baseline (skull outer 3D only)	Subject specific (skull outer 3D only)
								Test		Force (simulation)			Fracture (simulation)			
Hodgson 1971 & 1973	4	No (>1 test and injury)	Yes	Rigid	2.23	Front	0	6.4	1	9.2	9.2		1	0		
Hodgson 1971 & 1973	6	No (>1 test and injury)	Yes	Rigid	2.23	Front	0	5.4	1	9.2	9.2		1	0		
Hodgson 1971 & 1973	29	No (>1 test and injury)	Yes	Rigid	3.51	Front	0	7.9	1	14.1	16.0		1	1		
Hodgson 1971 & 1973	30	No (>1 test and injury)	Yes	Rigid	3.87	Front	0	7.5	1	14.2	17.1		1	1		
Hodgson 1971 & 1973	15	No (>1 test and injury)	Yes	Rigid	2.23	Front	0	7.3	1	7.3	7.2		1	0		
Hodgson 1971 & 1973	16	No (>1 test and injury)	Yes	Rigid	2.23	Front	0	4.2	1	7.3	7.2		1	0		
Hodgson 1971 & 1973	17	No (>1 test and injury)	Yes	Rigid	2.23	Front	0	8.0	1	7.3	7.2		1	0		
Hodgson 1971 & 1973	19	No (>1 test and injury)	Yes	Rigid	2.87	Front	0	7.3	1	9.2	10.0		1	1		
Hodgson 1971 & 1973	20	No (>1 test and injury)	Yes	Rigid	3.14	Front	0	8.9	1	9.7	11.1		1	1		
Hodgson 1971 & 1973	11	No (>1 test and injury)	Yes	Rigid	2.96	Front	0	9.0	1	8.0	9.5		1	1		
Hodgson 1971 & 1973	12	No (>1 test and injury)	Yes	Rigid	3.14	Front	0	6.1	1	8.5	10.3		1	1		
Hodgson 1971 & 1973	13	No (>1 test and injury)	Yes	Rigid	2.83	Front	0	8.8	1	8.5	8.9		1	1		
Hodgson 1971 & 1973	4	No (>1 test and injury)	Yes	Rigid	3.17	Front	0	7.1	1	7.5	9.9		1	1		
Hodgson 1971 & 1973	8	No (>1 test and injury)	Yes	Rigid	2.99	Front	0	8.3	1	7.4	9.1		1	1		
Hodgson 1971 & 1973	9	No (>1 test and injury)	Yes	Rigid	2.77	Front	0	5.9	1	7.3	8.1		0	1		
Hodgson 1971 & 1973	34	No (>1 test and injury)	Yes	Rigid	3.23	Front	0	6.9	1	5.6	8.7		1	1		
Hodgson 1971 & 1973	35	No (>1 test and injury)	Yes	Rigid	4.15	Front	0	6.2	1	6.7	11.0		1	1		

Reference	Test	Injury assessment	Force comp.	Impact. stiff.	Vel. (m/s)	Loc.	Angle (deg)	Force (kN)	Fx	Baseline (failure enabled)	Baseline (failure disabled)	Subject specific	Base.	Subject specific	Baseline (skull outer 3D only)	Subject specific (skull outer 3D only)
								Test		Force (simulation)			Fracture (simulation)			
Hodgson 1971 & 1973	1	No (>1 test and injury)	Yes	Rigid	2.96	Front	0	5.5	1	14.5	14.5		1	0		
Hodgson 1971 & 1973	2	No (>1 test and injury)	Yes	Rigid	3.29	Front	0	5.5	1	16.2	16.4		1	0		
Hodgson 1971 & 1973	3	No (>1 test and injury)	Yes	Rigid	3.51	Front	0	5.9	1	17.7	17.8		0	0		
Hodgson 1971 & 1973	5	No (>1 test and injury)	Yes	Rigid	2.93	Front	0	7.3	1	3.1	3.1		1	1		
Hodgson 1971 & 1973	6	No (>1 test and injury)	Yes	Rigid	3.05	Front	0	6.3	1	3.1	3.1		1	1		
Hodgson 1971 & 1973	7	No (>1 test and injury)	Yes	Rigid	3.05	Front	0	5.9	1	15.0	15.0		1	0		
Hodgson 1971 & 1973	10	No (>1 test and injury)	Yes	Rigid	3.32	Front	0	5.9	1	16.5	16.7		1	0		
Hodgson 1971 & 1973	31	No (>1 test and injury)	Yes	Rigid	2.87	Front	0	4.4	1	13.2	13.3		1	0		
Hodgson 1971 & 1973	32	No (>1 test and injury)	Yes	Rigid	3.14	Front	0	6.8	1	14.6	15.0		1	0		
Hodgson 1971 & 1973	33	No (>1 test and injury)	Yes	Rigid	3.14	Front	0	3.7	1	14.6	15.0		1	0		
Hodgson 1971 & 1973	34	No (>1 test and injury)	Yes	Rigid	3.14	Front	0	5.8	1	14.6	15.0		1	0		
Hodgson 1971 & 1973	35	No (>1 test and injury)	Yes	Rigid	3.51	Front	0	5.6	1	15.2	17.4		1	1		
Hodgson 1971 & 1973	14	No (>1 test and injury)	Yes	Rigid	3.23	Front	0	8.5	1	16.0	16.3		1	1		
Hodgson 1971 & 1973	15	No (>1 test and injury)	Yes	Rigid	3.14	Front	0	10.0	1	15.5	15.7		1	0		
Hodgson 1971 & 1973	16	No (>1 test and injury)	Yes	Rigid	3.54	Front	0	10.8	1	16.3	18.1		1	1		
Hodgson 1971 & 1973	21	No (>1 test and injury)	Yes	Rigid	2.87	Front	0	3.5	1	14.0	14.0		1	0		
Hodgson 1971 & 1973	22	No (>1 test and injury)	Yes	Rigid	2.87	Front	0	4.1	1	14.0	14.0		1	0		

Reference	Test	Injury assessment	Force comp.	Impact. stiff.	Vel. (m/s)	Loc.	Angle (deg)	Force (kN)	Fx	Baseline (failure enabled)	Baseline (failure disabled)	Subject specific	Base.	Subject specific	Baseline (skull outer 3D only)	Subject specific (skull outer 3D only)
								Test		Force (simulation)			Fracture (simulation)			
Hodgson 1971 & 1973	23	No (>1 test and injury)	Yes	Rigid	2.87	Front	0	3.3	1	14.0	14.0		1	0		
Hodgson 1971 & 1973	24	No (>1 test and injury)	Yes	Rigid	3.14	Front	0	4.0	1	15.7	15.7		1	0		
Hodgson 1971 & 1973	7	No (>1 test and injury)	Yes	Rigid	3.87	Temp.	0	8.9	1	17.5	18.8		1	1		
Hodgson 1971 & 1973	8	No (>1 test and injury)	Yes	Rigid	4.42	Temp.	0	14.9	1	19.1	21.4		1	1		
Hodgson 1971 & 1973	9	No (>1 test and injury)	Yes	Rigid	2.23	Temp.	0	2.4	1	10.3	10.5		1	0		
Hodgson 1971 & 1973	10	No (>1 test and injury)	Yes	Rigid	2.23	Temp.	0	4.7	1	10.3	10.5		1	0		
Hodgson 1971 & 1973	11	No (>1 test and injury)	Yes	Rigid	2.87	Temp.	0	5.2	1	13.8	13.9		0	0		
Hodgson 1971 & 1973	13	No (>1 test and injury)	Yes	Rigid	2.87	Temp.	0	5.6	1	13.8	13.9		0	0		
Hodgson 1971 & 1973	14	No (>1 test and injury)	Yes	Rigid	3.87	Temp.	0	13.3	1	17.5	18.8		0	1		
McIntosh et al. 1993	8549D	Yes (strongest w.o injury)	Yes	Ens.	3.6	Temp.	0	5.2	0	2.6	2.6		0	0		
McIntosh et al. 1993	8541D	Yes (strongest w.o injury)	Yes	Ens.	3.7	Temp.	0	5.3	0	2.8	2.8		1	0		
McIntosh et al. 1993	8539	Yes (1 test/PMHS)	Yes	Rigid	2.8	Temp.	0	4.9	0	12.9	13.0		1	0		
McIntosh et al. 1993	9208	Yes (1 test/PMHS)	Yes	Rigid	6	Temp.	0	11.7	1	26.8	26.8		1	1		
McIntosh et al. 1993	9209	Yes (1 test/PMHS)	Yes	Rigid	6.1	Temp.	0	11.5	1	26.9	26.9		1	1		
McIntosh et al. 1993	9211	Yes (1 test/PMHS)	Yes	Rigid	5.9	Temp.	0	11.0	1	26.1	26.1		0	1		
McIntosh et al. 1993	9213	Yes (1 test/PMHS)	Yes	Rigid	6.1	Temp.	0	7.5	0	26.9	26.9		0	1		
McIntosh et al. 1993	9221	Yes (1 test/PMHS)	Yes	Rigid	5.7	Temp.	0	9.1	0	25.1	25.1		0	1		

Reference	Test	Injury assessment	Force comp.	Impact. stiff.	Vel. (m/s)	Loc.	Angle (deg)	Force (kN)	Fx	Baseline (failure enabled)	Baseline (failure disabled)	Subject specific	Base.	Subject specific	Baseline (skull outer 3D only)	Subject specific (skull outer 3D only)
								Test		Force (simulation)			Fracture (simulation)			
McIntosh et al. 1993	9215D	Yes (strongest w.o injury)	Yes	Ens.	5.9	Temp.	0	7.4	0	10.1	10.1		1		0	
McIntosh et al. 1993	9217D	Yes (strongest w.o injury)	Yes	Ens.	5.9	Temp.	0	6.9	0	10.1	10.1		1		0	
McIntosh et al. 1993	9218D	Yes (strongest w.o injury)	Yes	Ens.	5.9	Temp.	0	7.9	0	10.1	10.1		1		0	
Nusholtz et al. 1984	82E001	Yes (1 test/PMHS)	Yes	Ens.	5	Front	0	9.1	1	11.3	11.3		1		0	
Nusholtz et al. 1984	82E022	Yes (strongest w.o injury)	Yes	Ens.	5.7	Front	0	9.6	0	16.5	16.5		1		0	
Nusholtz et al. 1984	82E042	Yes (strongest w.o injury)	Yes	Ens.	5.5	Front	0	10.2	0	15.0	15.0		1		0	
Nusholtz et al. 1984	82E062	Yes (strongest w.o injury)	Yes	Ens.	5.5	Front	0	9.6	0	15.0	15.0		0		0	
Nusholtz et al. 1984	82E082	Yes (strongest w.o injury)	Yes	Ens.	3.8	Front	0	4.1	0	4.1	4.1		1		0	
Raymond et al. 2009	2426R	Yes (1 test/side)	Yes	Rigid	22.2	Temp.	0	3.0	0	9.2	9.3	8.90	1	1	0	0
Raymond et al. 2009	2908R	Yes (1 test/side)	Yes	Rigid	19.6	Temp.	0	3.7	0	8.2	8.3	7.64	1	1	0	0
Raymond et al. 2009	2904R	Yes (1 test/side)	Yes	Rigid	17.3	Temp.	0	3.2	0	7.2	7.2	7.14	0	0	0	0
Raymond et al. 2009	2939L	Yes (1 test/side)	Yes	Rigid	16.3	Temp.	0	2.5	0	6.8	6.8	5.19	0	0	0	0
Raymond et al. 2009	2965L	Yes (1 test/side)	Yes	Rigid	18	Temp.	0	3.6	0	7.6	7.6	5.94	0	0	0	0
Raymond et al. 2009	2427R	Yes (1 test/side)	Yes	Rigid	23.4	Temp.	0	6.3	1	9.9	9.9	10.18	1	1	0	1
Raymond et al. 2009	2978L	Yes (1 test/side)	Yes	Rigid	19.5	Temp.	0	3.4	1	8.2	8.2	6.54	1	1	0	0
Raymond et al. 2009	2426L	Yes (1 test/side)	Yes	Rigid	32.1	Temp.	0	5.7	1	12.9	13.1	12.64	1	1	1	1
Raymond et al. 2009	2427L	Yes (1 test/side)	Yes	Rigid	34.2	Temp.	0	9.5	1	13.5	13.7	13.62	1	1	1	1

Reference	Test	Injury assessment	Force comp.	Impact. stiff.	Vel. (m/s)	Loc.	Angle (deg)	Force (kN)	Fx	Baseline (failure enabled)	Baseline (failure disabled)	Subject specific	Base.	Subject specific	Baseline (skull outer 3D only)	Subject specific (skull outer 3D only)
								Test		Force (simulation)			Fracture (simulation)			
Raymond et al. 2009	2908L	Yes (1 test/side)	Yes	Rigid	35.1	Temp.	0	4.7	1	13.9	14.2	14.28	1	1	1	1
Raymond et al. 2009	2904L	Yes (1 test/side)	Yes	Rigid	31.9	Temp.	0	6.0	0	12.8	13.0	13.53	1	1	1	1
Raymond et al. 2009	2939R	Yes (1 test/side)	Yes	Rigid	34.4	Temp.	0	5.0	0	13.8	13.9	11.60	1	1	1	0
Raymond et al. 2009	2965R	Yes (1 test/side)	Yes	Rigid	35.2	Temp.	0	6.2	1	13.9	14.1	15.70	1	1	1	1
Raymond et al. 2009	2978R	Yes (1 test/side)	Yes	Rigid	32.4	Temp.	0	3.5	1	13.0	13.1	11.99	1	1	1	1
Stark et al. 2019	9	Yes (strongest w.o injury)	No data	Drone	21.4	Front	58		0	12.0	12.0	3.74	0	0	0	0
Stark et al. 2019	11a	Yes (strongest w.o injury)	No data	Drone	21.9	Par.	58		0	13.2	13.2	5.01	0	0	0	0
Stark et al. 2019	19	Yes (strongest w.o injury)	No data	Drone	21.9	Front	58		0	12.3	12.3	12.00	0	0	0	0
Stark et al. 2019	21	Yes (strongest w.o injury)	No data	Drone	21.3	Front	58		0	2.5	2.5	2.35	0	0	0	0
Stark et al. 2019	31	Yes (least with fracture)	No data	Rigid	5.7	Temp.	0		0	11.3	11.4	10.78	1	1	0	0
Yoganandan et al. 1995	7	No (imposed disp.)	Yes	Rigid	7.2	Top	0	14.0	1	19.2			1		1	
Yoganandan et al. 1995	8	No (imposed disp.)	Yes	Rigid	7.1	Front	45	13.6	1	19.3			1		1	
Yoganandan et al. 1995	9	No (imposed disp.)	Yes	Rigid	7.6	Top	0	13.6	1	19.0			1		1	
Yoganandan et al. 1995	10	No (imposed disp.)	Yes	Rigid	7.3	Rear	35	10.0	1	20.3			1		1	
Yoganandan et al. 1995	11	No (imposed disp.)	Yes	Rigid	7.8	Top	0	8.8	1	19.2			1		1	
Yoganandan et al. 1995	12	No (imposed disp.)	Yes	Rigid	8	Top	0	11.6	1	19.2			1		1	
Sum	218	156	175						129				156	12/19	100	7/19

APPENDIX B. EXPANDED POLYSTYRENE AND ENSOLITE MODELS

Properties and tests of Expanded Polystyrene (EPS) and Ensolite are reported in the literature. However, there are typically not available at the very high strains / stress required for head impacts. If considering the different mechanisms described in Melvin and Evans (1971), pressures superior to 10 MPa (1500 psi) could be desirable to cover the scenario of comminuted and linear fractures.

Therefore, to complement literature data at high compression levels, samples were tested between two plates at low speed on a material testing machine. The compression was stopped at a force limit of approximately 10 kN to ensure a high compression and stress of the sample. Force and displacements were used to compute the engineering strain and stress using the initial geometry measured with a caliper. The samples were weighted to compute the density. The results were used to complement literature data.

For the polystyrene, Got et al. (1978) used medium density (21 and 25 kg/m3) expanded polystyrene (EPS) in their tests. Andena et al. (2018) tested EPS samples at various densities (including 19, 21, 25 kg/m3) and strain rates. They showed the limited effect of strain rate on EPS 19 kg/m3 but stopped their tests around 2 MPa. For this study, two 20x20x20 mm3 samples of 19 kg/m3 density were tested. While their initial response was slightly softer than Andena's perhaps due to the imperfect cut of the samples, their responses become similar around 0.8 strain and then extended until 27 MPa, i.e. much beyond Andena range (Figure 24). Therefore, the initial response of Andena was combined with the test results are high strain to build an idealized curve which was then scaled to the other densities (21 and 25 kg/m3). In the end, the difference between the densities is marginal when considering the complete strain range (Figure 25).

The same approach was used for the Ensolite. Three samples (nominal dimensions: 20x20x14 mm3) cut from a Hybrid III sternum pad were tested in the same conditions. Their density was 125 kg/m3. Their response, which was close from one another, was compared to Schwitzer et al. (2016). The low strain range of Schwizer was combined with the high strain range of the tests to build an idealized curve for the simulations (Figure 26).

References:

Andena, L., Caimmi, F., Leonardi, L., Nacucchi, M., and De Pascalis, F. (2019). Compression of polystyrene and polypropylene foams for energy absorption applications: A combined mechanical and microstructural study. *Journal of Cellular Plastics 55*, 49–72. https://doi.org/10.1177/0021955X18806794.

Melvin, J. W., & Evans, F. G. (1971). A Strain Energy Approach to the Mechanics of Skull Fracture. *15th Stapp Car Crash Conference (1971)*, 710871. https://doi.org/10.4271/710871

Schwizer, P., Demierre, M., and Smith, L.V. (2016). Evaluation of Catcher Mask Impacts. *Procedia Engineering 147*, 228–233. https://doi.org/10.1016/j.proeng.2016.06.218.

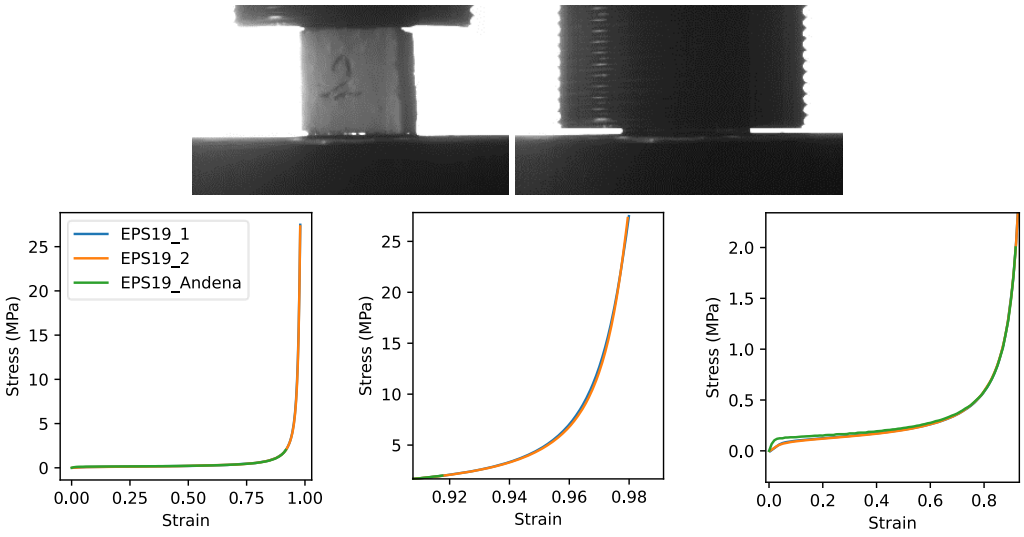

Figure 24. EPS compression just before contact and at peak compression (top) and response curves (bottom) compared to Andena's test. The curves from the two samples are almost superimposed. The plots represent different zoom levels on the same curves.

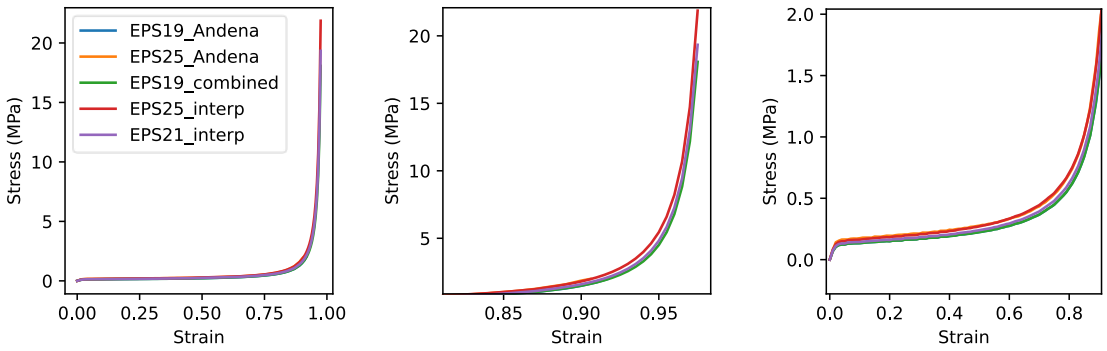

Figure 25. Interpolation at 21 and 25 kg/m^3 based on the combination of Andena and current tests scaled to the sample tests from Andena for these densities. The plots represent different zoom levels on the same curves.

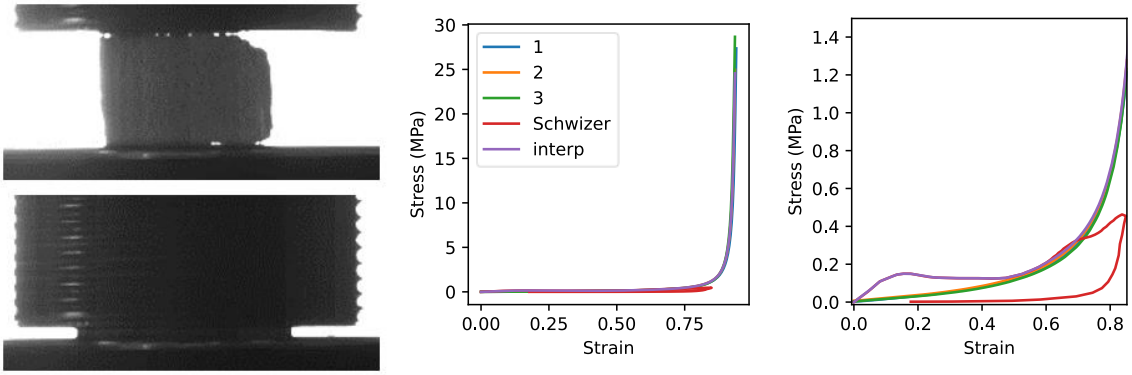

Figure 26. Ensolite test (samples 1,2,3) and comparison and combination with Schwizer. The plots represent different zoom levels on the same curves.

APPENDIX C. SIMPLIFIED DRONE MODELS

Two simplified models of drones used in Stark et al. (2019) were developed for the current study: (1) a DJI Phantom 3 and (2) a DJI Mavic Pro. By simplified, it is meant that the objective was not to reproduce the exact material and response of individual components and their assembly (as in the ASSURE project) but to have a model representing the main structures that would be able to load the head in a similar manner as the physical drone in specific configurations: an impact on the side of the Mavic and an impact to the front of the Phantom. This involves simplifications making the models are specific to the configurations tested (e.g. the drone of the Mavic are tied to the body as they do not rotate during the target tests). The models can be shared upon request for research use and may be open sourced in the future depending on legal implications.

In practice, actual drones were taken apart, scanned and their components weighted. Then, simplified meshes of the main components were developed and assembled in a comparable way as in the drone (Figure 27). Elastoplastic material properties were used, separating the materials by broad type and usage (metal, motherboard, battery cell, body, etc.). Motors were rigid. Their densities were set, and their material parameter adjusted until the response of calibration tests can be approached.

Two types of tests were used:

1. Calibration tests were performed at Onera by launching the drones against a rigid surface shaped as the forehead of a Hybrid III skull (without foam). The kinematics and reaction forces were recorded. The material properties were adjusted by comparison against these tests.
2. Verification tests, in which the drone models were launched at a Hybrid III head (with foam). For the Mavic, tests performed at Univ Eiffel for this project were used. For the Phantom 3, tests performed by NIAR performed within the ASSURE project were used.

Illustrations of the procedure and results are shown hereafter.

The main focus was the Phantom as it could have been close to an injurious condition in Stark et al. and was used in several simulations. Two rigid test conditions (calibration), with the drone oriented slightly differently, were simulated. The slight difference in angle led to a different involvement of the drone components (camera in particular) which affected the response. The force could be approximated in both cases with the same model (Figure 28) and loading of an actual dummy head also lead to similar head accelerations (Figure 29). Although the model does not describe the response of individual components (which were not validated separately), it was deemed sufficient to apply a load on a head shape. The same approach was used for the Mavic, with the response against the rigid shape development tests and dummy head verification tests summarized in Figure 30 and Figure 31.

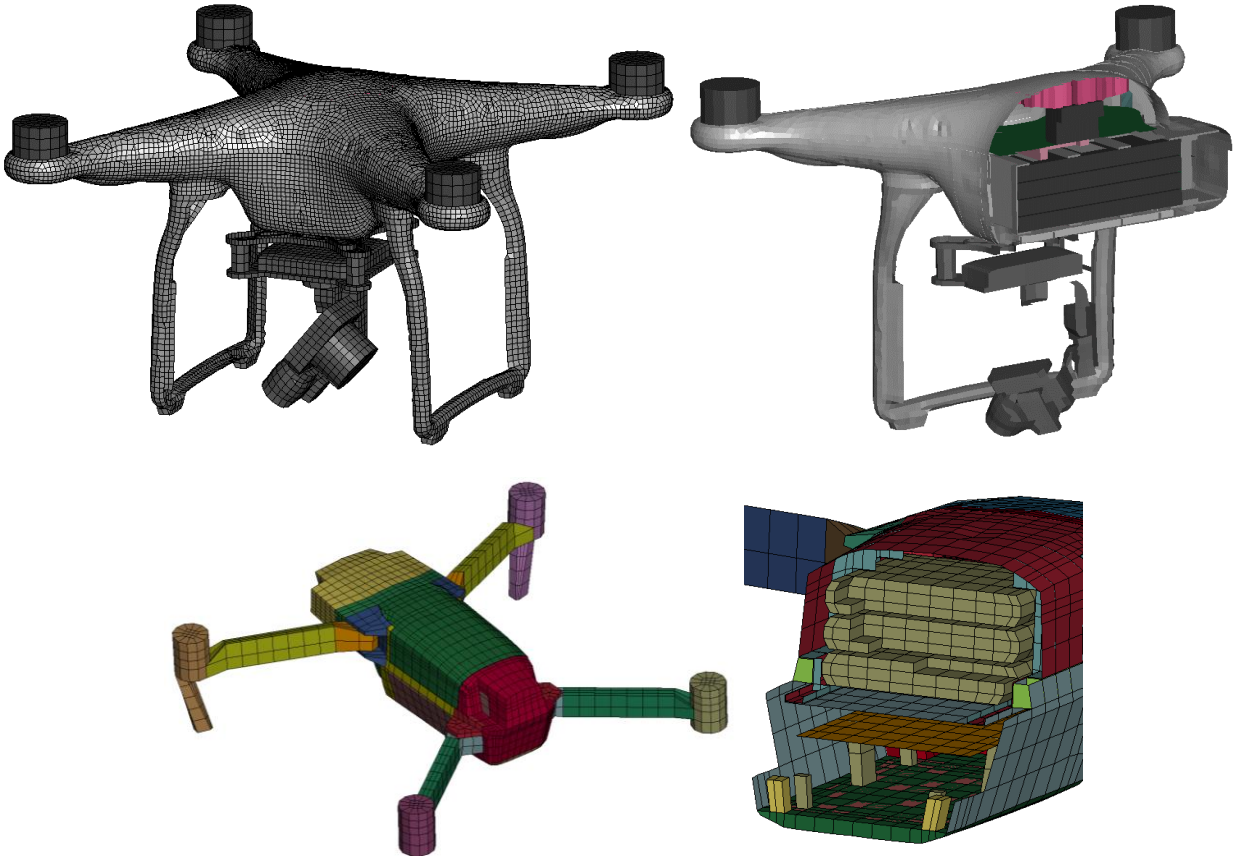

Figure 27. Mesh of the Phantom 3 (top) and Mavic (bottom) with their components. The four cell (Phantom) and three cell (Mavic) batteries are visible on the section on the right.

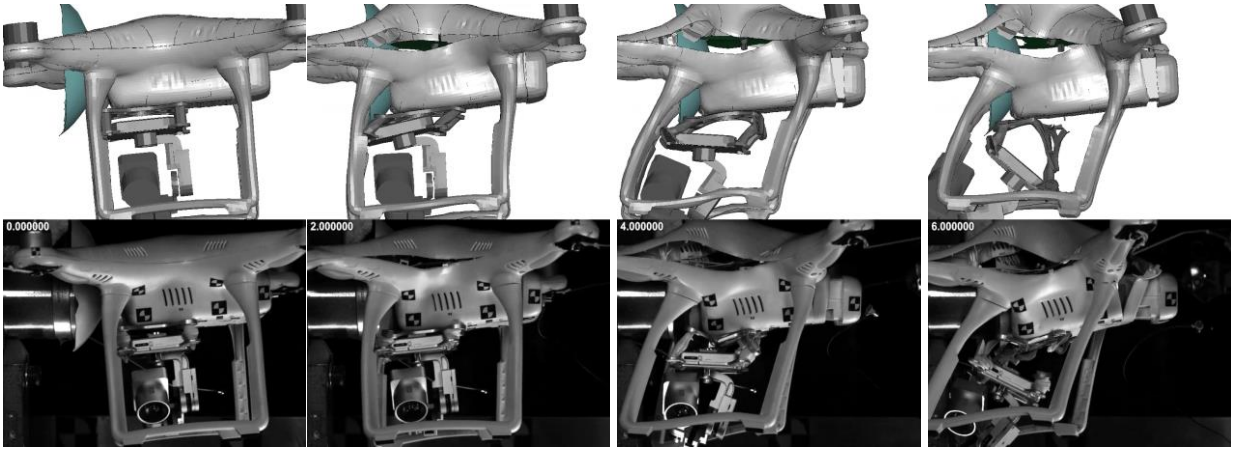

a) Kinematics in the configuration called nominal

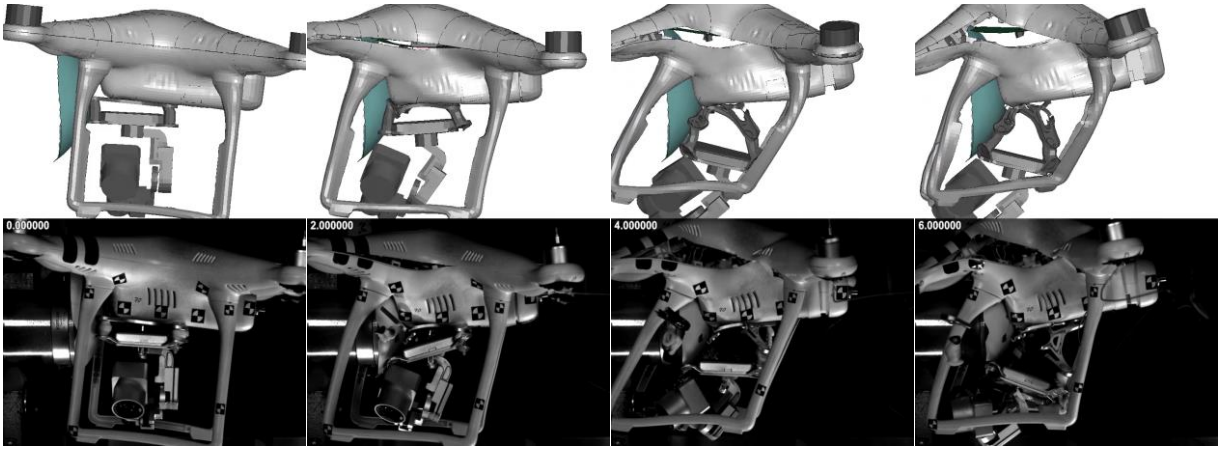

b) Kinematics in the configuration called Stark

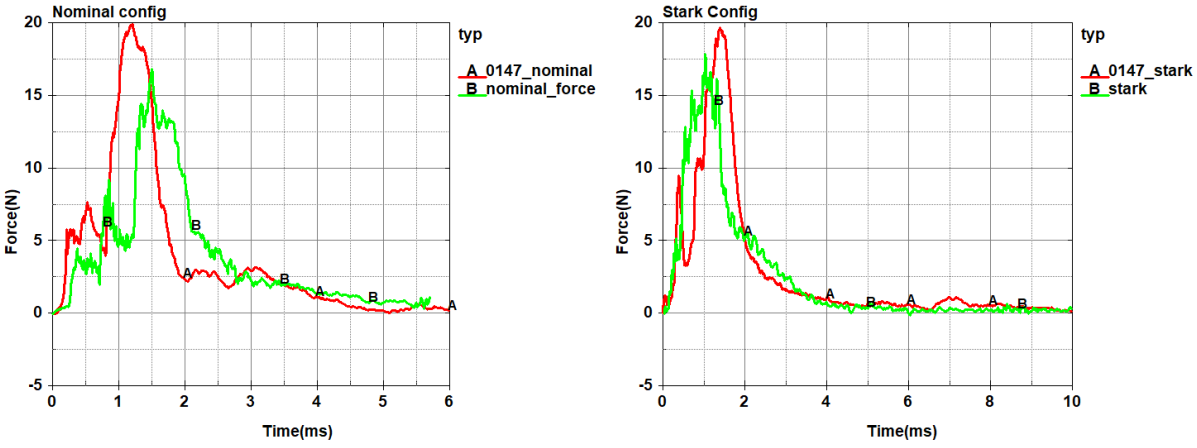

a) Forces in the tests (green) vs simulations (red) for the two configurations

Figure 28. Phantom 3 simplified model against the drone calibration tests performed at Onera (speed 21.8m/s against rigid shape).

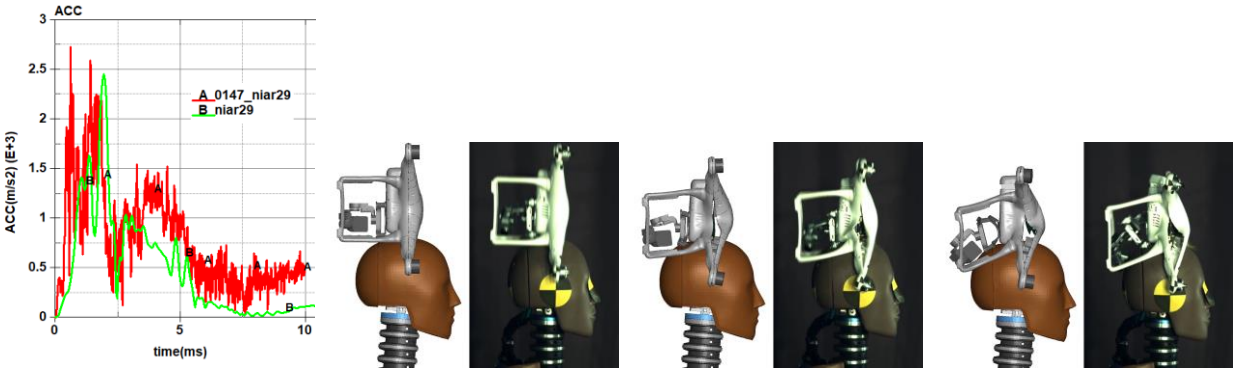

a) Niar 29 test: kinematics and head CG acceleration (model in red)

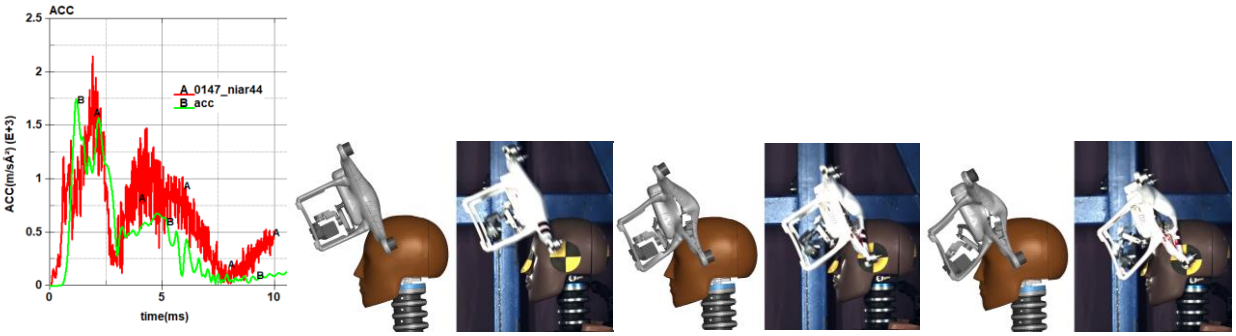

b) Niar 44 test: kinematics and head CG acceleration (model in red)

Figure 29. Phantom 3 simplified model checkup against two tests performed at NIAR for the ASSURE project.

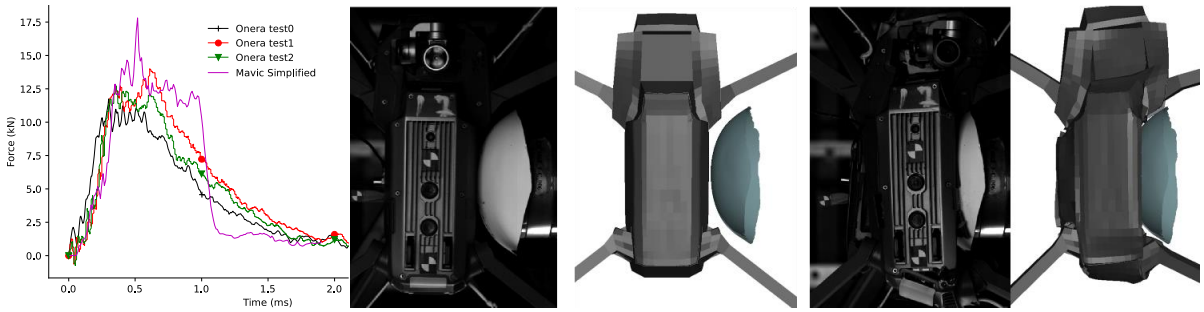

Figure 30. Mavic simplified model against the drone calibration tests performed at Onera (speed 21.1m/s against rigid shape).

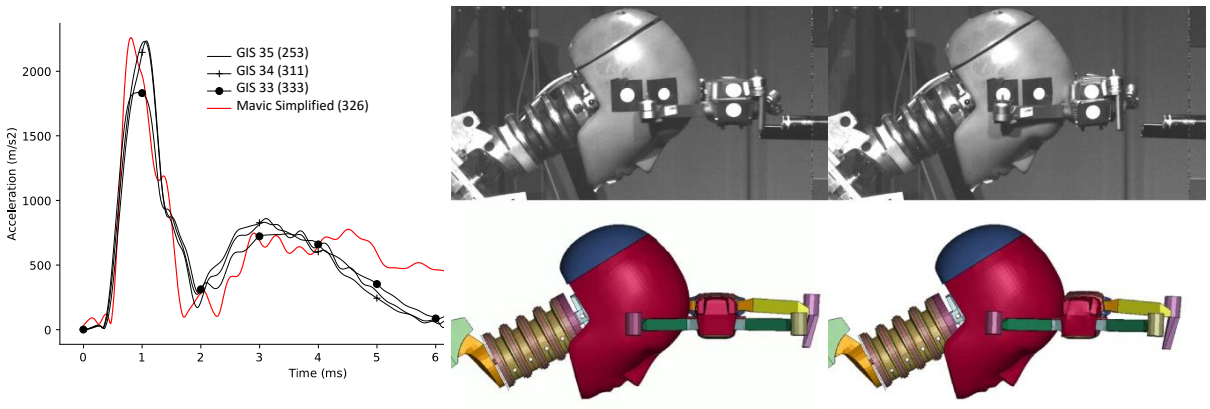

Figure 31. Mavic simplified model checkup against a dummy at 15m/s (3 tests performed at Univ Eiffel). The number in parenthesis is the HIC.

APPENDIX D. COMPARISON BETWEEN HEAD-NECK AND FULL BODY SETUP

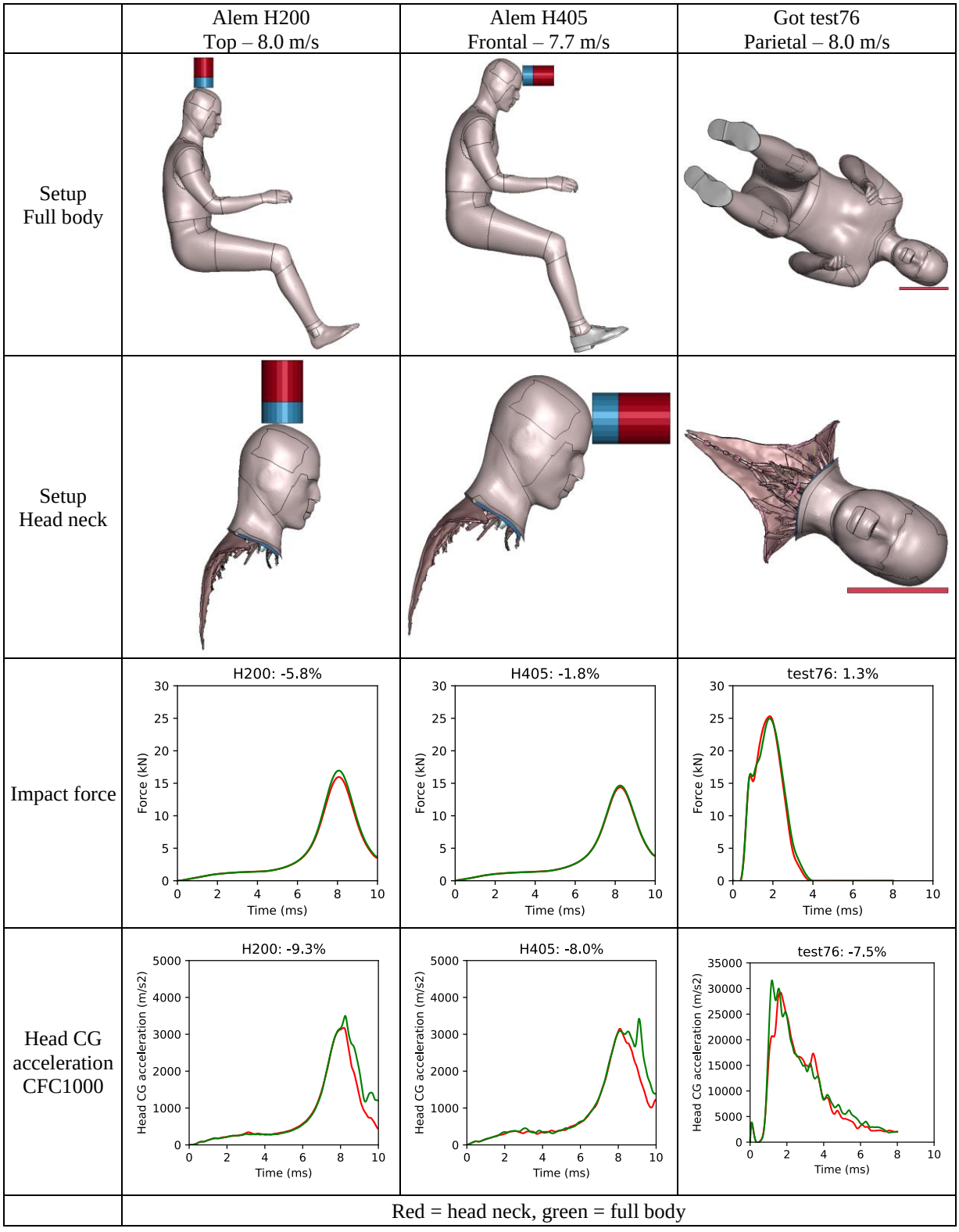

Figure 32. Comparison between full-body and head-neck setups in the simulations: configuration, impact forces and head CG acceleration. The percentages in the graph's titles correspond to the peak differences from the full body to the head neck setup.